ORNL/TM-2022/2728

Progress on Associated-Particle Imaging Algorithms, 2022

P. A. Hausladen
M. R. Heath
R. J. Newby
P. B. Rose
J. Gregor
A. J. Gilbert
L. A. Campbell
N. Deshmukh
R. S. Wittman
J. K. Mattingly
M. Lockhart

Approved for public release.
Distribution is unlimited.

September 2022

OAK RIDGE
National Laboratory

ORNL IS MANAGED BY UT-BATTELLE LLC FOR THE US DEPARTMENT OF ENERGY

DOCUMENT AVAILABILITY

Reports produced after January 1, 1996, are generally available free via OSTI.GOV.

Website www.osti.gov

Reports produced before January 1, 1996, may be purchased by members of the public from the following source:

National Technical Information Service
5285 Port Royal Road
Springfield, VA 22161
Telephone 703-605-6000 (1-800-553-6847)
TDD 703-487-4639
Fax 703-605-6900
E-mail info@ntis.gov
Website http://classic.ntis.gov/

Reports are available to US Department of Energy (DOE) employees, DOE contractors, Energy Technology Data Exchange representatives, and International Nuclear Information System representatives from the following source:

Office of Scientific and Technical Information
PO Box 62
Oak Ridge, TN 37831
Telephone 865-576-8401
Fax 865-576-5728
E-mail reports@osti.gov
Website https://www.osti.gov/

This report was prepared as an account of work sponsored by an agency of the United States Government. Neither the United States Government nor any agency thereof, nor any of their employees, makes any warranty, express or implied, or assumes any legal liability or responsibility for the accuracy, completeness, or usefulness of any information, apparatus, product, or process disclosed, or represents that its use would not infringe privately owned rights. Reference herein to any specific commercial product, process, or service by trade name, trademark, manufacturer, or otherwise, does not necessarily constitute or imply its endorsement, recommendation, or favoring by the United States Government or any agency thereof. The views and opinions of authors expressed herein do not necessarily state or reflect those of the United States Government or any agency thereof.

ORNL/TM-2022/2728

Physics Division

ROGRESS ON ASSOCIATED-PARTICLE IMAGING ALGORITHMS, 2022

P. A. Hausladen
M. R. Heath
R. J. Newby
P. B. Rose
J. Gregor
A. J. Gilbert
L. A. Campbell
N. Deshmukh
R. S. Wittman
J. K. Mattingly
M. Lockhart

September 2022

Prepared by
OAK RIDGE NATIONAL LABORATORY
Oak Ridge, TN 37831
managed by
UT-BATTELLE LLC
for the
US DEPARTMENT OF ENERGY
under contract DE-AC05-00OR22725

CONTENTS

LIST OF FIGURES

LIST OF TABLES

ABBREVIATIONS

API	associated-particle imaging
ART	Algebraic Reconstruction Technique
D-T	deuterium–tritium
DU	depleted uranium
HEU	highly enriched uranium
MCNP	Monte Carlo N-Particle
MVp	megavolt peak
NCSU	North Carolina State University
ORNL	Oak Ridge National Laboratory
OS	ordered subsets
PSF	point spread function
RMSE	root mean square error
SIRT	simultaneous iterative reconstruction technique
SNR	signal-to-noise ratio
TOF	time of flight
TV	total variation
WLS	weighted least squares
Z	atomic number

ACKNOWLEDGMENTS

This work is supported by the US Department of Energy, Office of Defense Nuclear Nonproliferation Research and Development in the National Nuclear Security Administration (NA-22).

ABSTRACT

The present work describes progress on developing imaging algorithms that use fast neutron signatures acquired using the associated-particle imaging (API) method. The present work complements ongoing work to develop neutron source and detector hardware to enable field inspection by investigating algorithms that can discriminate among critical materials or extract 3D geometrical information from single-sided or transmission measurements. The present work has three focus areas:

1. Iterative reconstruction of inelastic gamma-ray emissions to perform 3D time-of-flight (TOF) imaging in a single view in either transmission or backscatter configurations. Iterative reconstruction enables better image resolution than the inherent TOF resolution.

2. Decomposition of registered neutron and x-ray radiographs into an assumed material list for each pixel in the image.

3. Material identification using full spectral analysis that includes the emergent neutron and gamma-ray energies, times, and angles.

Progress for each approach is summarized for FY 2022.

1. INTRODUCTION

This document reports progress on the development of three approaches to analysis of API imaging data for FY 2022. Progress for previous years (FY 2020 and FY 2021) is documented in reports for those years [1, 2], but introductory wording is shared largely unchanged by the present report. The present report satisfies the FY 2022 technical deliverable “Progress Report on Algorithms, FY 2022,” for the project “Associated-Particle Imaging Algorithms for Material Identification” supported by the US Department of Energy’s Office of Defense Nuclear Nonproliferation Research and Development.

For the past decade, the US Department of Energy’s Oak Ridge National Laboratory (ORNL) has developed 3D tomographic imaging techniques using fast neutrons from a deuterium–tritium (D-T) neutron generator produced via the $d + t \rightarrow \alpha + n$ reaction. This development has focused on the API technique, in which the time and location of detected alpha particles (ascertained by a detector embedded in the D-T neutron generator) determine the time and direction of the associated 14.1 MeV neutrons. Using API techniques, transmission imaging with excellent contrast using a wide-cone beam can be achieved. Induced-reaction imaging techniques that can reconstruct images of the probability of induced fission and hydrogen elastic scattering are also possible. In these induced-reaction imaging modalities, the lines of response are determined by the initial directions of the interrogating neutrons as determined by their associated alpha-particle positions (pixels). Progress has also been made on developing imaging techniques in which the contrast originates from small-angle scattering and inelastic neutron scattering (reconstructing based on either detected gamma rays or detected neutrons).

To date, efforts toward developing imaging techniques have concentrated on tomographic measurements using laboratory imaging systems with gantries that position the source and detector with respect to each other. For these imaging techniques, image reconstruction does not correspond to uniquely identifying materials and densities for each voxel in the image. Rather, image reconstruction corresponds to reconstructing a single parameter for each voxel of the image. In transmission images, that parameter is the attenuation coefficient, which can be interpreted as the total probability of a neutron interacting per centimeter. For induced-fission imaging, the parameter is the number of neutron pairs produced per centimeter per incident neutron. A further complication of reconstructing induced-reaction images is that inferring physical values for voxels in the image requires knowledge of the reconstructed 3D transmission through the volume to correct for efficiency.

The present work is part of an effort to transition imaging using D-T neutrons from laboratory use to field use by enabling a portable inspection capability. In this use case, the source and detector will be hand-positioned, and imaging will be limited to a single or few views. In some instances, transmission imaging may not be possible. Other efforts address the source and detector hardware to reduce their size, power, and complexity to the operator. The present work addresses algorithm development to extract maximum information from the available API signatures in the context of single or few-view measurements. This algorithm work can be categorized into the following two general themes.

1. Algorithms that directly calculate images from data with a minimum of assumptions to give operators the best estimate of a 3D object geometry from a single measurement. In this case, images are voxel maps in which each voxel value corresponds to the probability of a given interaction and may be calculated from data in either transmission or backscatter measurement geometries.

2. Algorithms that directly reconstruct for materials and densities (rather than a parameter that encodes the probability of a particular reaction) but may have constraints on the materials or geometry to make the optimization problem tractable.

The present work investigates the following three distinct approaches that address these themes:

- Iterative TOF reconstruction of inelastic gamma-ray emissions. This approach reconstructs the probability of inducing inelastic gamma rays per incident neutron in each voxel of an image. Because the speeds of 14 MeV neutrons and gamma rays are known, performing 3D TOF reconstruction in a single view in either transmission or backscatter configurations is possible. Iterative reconstruction enables better image resolution than the inherent TOF resolution.

- Decomposition of x-ray and neutron transmission into a materials basis. This approach uses transmission imaging of D-T neutrons and high-energy x-rays to reconstruct a best-fit decomposition to an assumed material list for each pixel in registered neutron and x-ray radiographs. Including additional API observables is planned for future efforts.

- Material identification using full spectral analysis. The goal of this approach is to make a best estimate of the materials in an inspected object of known geometry by simultaneously fitting all possible API signatures. The initial thrust of this effort is to identify a way to implement a forward model that is sufficiently fast and that calculates all the desired signatures.

The three approaches are reported in Sections 2, 0, and 4.

2. ITERATIVE GAMMA-RAY TOF RECONSTRUCTION

Imaging the distribution of inelastic-scattering gamma rays produced in an object by the passage of interrogating D-T neutrons is desirable because the known speeds of 14 MeV neutrons and gamma rays make 3D TOF reconstruction possible in a single view when the source and detectors are positioned in either a transmission or a backscatter configuration. Several authors have previously investigated this form of imaging by using spectroscopic gamma ray detectors primarily to quantify the carbon, nitrogen, and oxygen in cargo to screen for the presence of explosives [3].

ORNL began investigating iterative reconstruction of TOF images of inelastic gamma rays induced by 14 MeV D-T neutrons in the Fast TOF Correlation project performed in collaboration with Lawrence

Livermore National Laboratory. In this work, gamma ray detection was performed by fast organic scintillator neutron detectors that were used primarily for multiplicity counting but are sensitive to gamma rays and allow for fast timing. Significantly, this work demonstrated that iterative reconstruction that exploits knowledge of the system response could achieve better spatial resolution than the intrinsic resolution given by TOF [4]. However, after these initial investigations, the ORNL effort on the Fast TOF Correlation project shifted to concentrate on developing a fast-timing neutron imaging panel. Investigation of iterative reconstruction shifted to the present work.

In other previous work, ORNL collaborated with the University of Tennessee, Knoxville, on the 3D Tomography and Image Processing Using Fast Neutrons project to combine modern parallel iterative reconstruction techniques with novel associated-particle, fast-neutron–induced reaction (induced fission and elastic scatter) and transmission imaging methods [5]. The resulting reconstruction code for novel imaging techniques achieved sufficient speed for practical 3D image reconstruction, approached favorable solutions using regularization and constraints, and weighted data by appropriate errors. The present work uses the building blocks of this existing 3D tomographic reconstruction code to implement 3D reconstruction of inelastic gamma ray emissions that is sufficiently fast and produces good images that have smooth sections with sharp edges.

2.1 HIGH-LEVEL SUMMARY OF FY 2020–2021 EFFORTS

Reconstruction of inelastic gamma rays is based on solving a regularized weighted least squares (WLS) problem subject to an optional total variation (TV) constraint:

$$\psi(x) = |Ax - y|_W^2 + \beta|x|^2$$

$$x^* = \operatorname{argmin}\, \psi(x) \ \text{ such that } \mathrm{TV}(x) < \varepsilon$$

Matrix A models the system geometry and physics associated with the induced gamma reactions; matrix W implements statistical weighting; and vectors x and y represent the image being reconstructed and the acquired projection data, respectively, as reported previously [1,2]. Each equation in the linear system represents what happens to neutrons as they travel in the direction of an alpha ray from the D-T source toward the detector array. The effect of constraining the TV value of the image is sparsification of the gradient magnitude image. This sparsification leads to solutions with smoother regions and more well-defined edges.

The WLS-TV problem is solved using a relaxed incremental proximal gradient scheme that consists of a two-step iteration [6,7]. First, the WLS term is minimized using a proximal mapping that keeps the image somewhat close to the one produced in the previous iteration. Next, the TV constraint is satisfied by mapping the image to the closest image with TV equaling the constraint using the Chambolle–Pock algorithm for solving convex optimization problems [8]. The core computation of the WLS minimization is a preconditioned gradient descent based on the simultaneous iterative reconstruction technique (SIRT) [9]:

$$x^{k+1} = \left[x^k - \alpha\, \tilde{C}\, \nabla\psi\left(x^k\right)\right]_+$$

The relaxation parameter α controls the step size, and over-relaxation is based on $\alpha \simeq 2$ being a near-optimal choice for ensuring fast convergence. Matrix $\tilde{C}$ is a carefully designed diagonal preconditioner. The projection operator $[\ ]_+$ sets negative values equal to 0. The implemented version includes Tikhonov regularization.

The bulk of the FY 2020–2021 efforts revolved around refactoring the multiview tomography code to the single-view geometry considered here and implementing the system model for the inelastic gamma rays. Two methods for accelerating the computation were implemented: (1) incremental widening of the timing window and (2) processing the alpha rays using an ordered subsets (OS) scheme. The algebraic reconstruction technique (ART) was studied as an alternative to SIRT but was abandoned because of difficulties with an effective parallel implementation. A faster implementation of SIRT was left for FY 2022. Experimental work confirmed that images can be produced that clearly indicate whether a depleted uranium (DU) ball is present inside a DU cylinder. However, the shape and appearance of the ball and the cylinder walls were not as round and uniform as expected. Compensation schemes were investigated, including but not limited to interpolation of central alpha rays, but they did not alleviate the problem. Finding a solution was left for FY 2022.

2.2 HIGH-LEVEL SUMMARY OF FY 2022 PROGRESS

2.2.1 Faster SIRT Implementation

FY 2022 efforts addressed speed-up of SIRT first by implementing TOF-based initialization and then by adding momentum-based acceleration. Because no benefits were realized from TOF-based initialization, it was discarded from further consideration. By contrast, momentum-based acceleration led to substantial improvements.

Momentum can be used to smooth stochastic variations while continuing to update regions where the gradient is near zero. In its simplest form, momentum incorporates a fraction γ of the previous update to the current update. For SIRT, this update translates as

$$x^{k+1} = x^k - \alpha\, \tilde{C}\, \nabla\psi\left(x^k\right) + \gamma\left(x^k - x^{k-1}\right)$$

Nesterov [10] proposed a momentum-like method that accelerates gradient descent to achieve the optimal rate of convergence. This method is widely used in machine learning for training of neural networks, but Kim et al [11] were the first to apply the method to image reconstruction. Initially, a standard gradient descent is performed, but from then on, a momentum step is applied before the gradient descent; the momentum step moves the update closer to the solution, and the gradient descent both updates and makes corrections needed to prevent overshooting. Standard gradient descent has an error bound of $O(1/k)$, whereas Nesterov's method, which does not guarantee monotonicity, has an error bound of $O(1/k^2)$.

Given $z^0 = x^0$ and $t_0 = 1$, the preconditioned gradient descent is modified as follows:

$$x^{k+1} = \left[z^k - \frac{1}{L}\tilde{C}\, \nabla\psi\left(z^k\right) \right]_+$$

$$t_{k+1} = \tfrac{1}{2}\left(1 + \sqrt{1 + 4t_k^2}\right)$$

$$z^{k+1} = x^{k+1} + \frac{t_k - 1}{t_{k+1}}\left(x^{k+1} - x^k\right)$$

The Lipschitz constant L is equal to the largest eigenvalue of the Hessian. The approximation $L \approx \lambda_{max}\left(\tilde{C}A^TWA\right) + \lambda_{max}\left(\beta\tilde{C}\right) = 1 + \max\left(\beta\tilde{C}\right)$ was used here. Choosing β such that $\max\left(\beta\tilde{C}\right) = 0.01$, yields $L \approx 1.01$. The resulting algorithm is referred to as SIRT WLS N1.

Kim and Fessler [12] introduced additional momentum capable of 2× faster convergence. Shown later to be equivalent to over-relaxation [13], the secondary sequence $\{z^k\}$ update can be expressed as

$$z^{k+1} = x^{k+1} + \frac{t_k - 1}{t_{k+1}}\left(x^{k+1} - x^k\right) + \sigma \frac{t_k}{t_{k+1}}\left(x^{k+1} - z^k\right)$$

An adaptive restart scheme resets $t_k = 1$ when the negative gradient and momentum vectors pull in opposite directions [14]. The scaling factor σ automatically decreases the over-relaxation to prevent overshooting of $\{z^k\}$, which can slow convergence and even lead to divergence. This modification of the iterative update allows increasing the over-relaxation when progress is being made. The resulting algorithm is referred to as SIRT WLS N2.

Figure 1 shows the WLS error reduction for SIRT WLS as well as SIRT WLS N1 and N2 for one, two, and four OS. Although SIRT WLS appears to converge to the same WLS error, the image nonetheless is blurrier than those produced by SIRT WLS N1 and N2. Comparison of the WLS error for the latter reveals that N1 converges more slowly than N2 but perhaps not by 2× because of the reduction of the additional momentum. Without this reduction, SIRT WLS N2 would have diverged for OS = 4. The TV constraint was applied after iteration 40 using a 0.50 cm full width half maximum blurring kernel to determine the threshold.

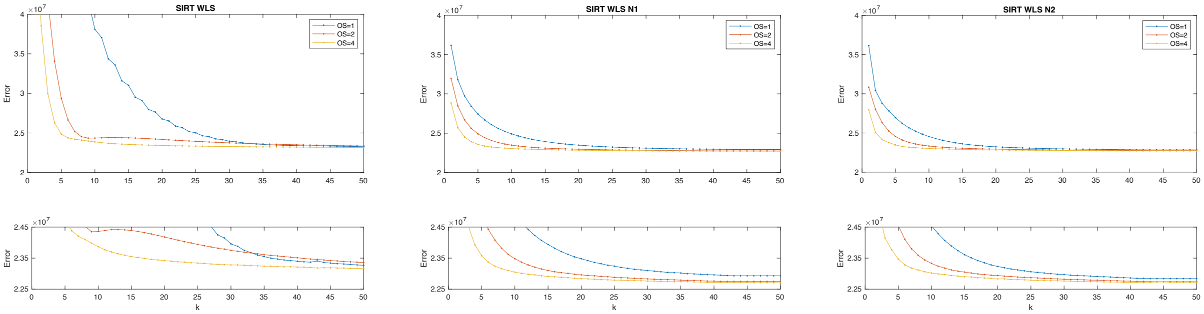

Figure 1. WLS error reduction for SIRT WLS and SIRT WLS N1 and N2.

Figure 2 shows slice 69 of the 3D image volumes produced by the three algorithms after 20 iterations using OS = 4. The images have been cropped to 0–12,000 counts. Calibration is needed to give the values physical meaning. After 20 and 50 iterations, the SIRT WLS image is visibly blurrier than the SIRT WLS N1 and N2 images. The SIRT WLS N1 and N2 results at 20 and 50 iterations are very similar. The DU ball within the cylinder is clearly visible in the SIRT WLS N1 and N2 images but the ball still appears elongated, and the cylinder walls distorted and discontinuous. The underlying cause of these aberrations in the images is thought to be due to inaccuracy of timing calibration as discussed in Section 2.2.3.

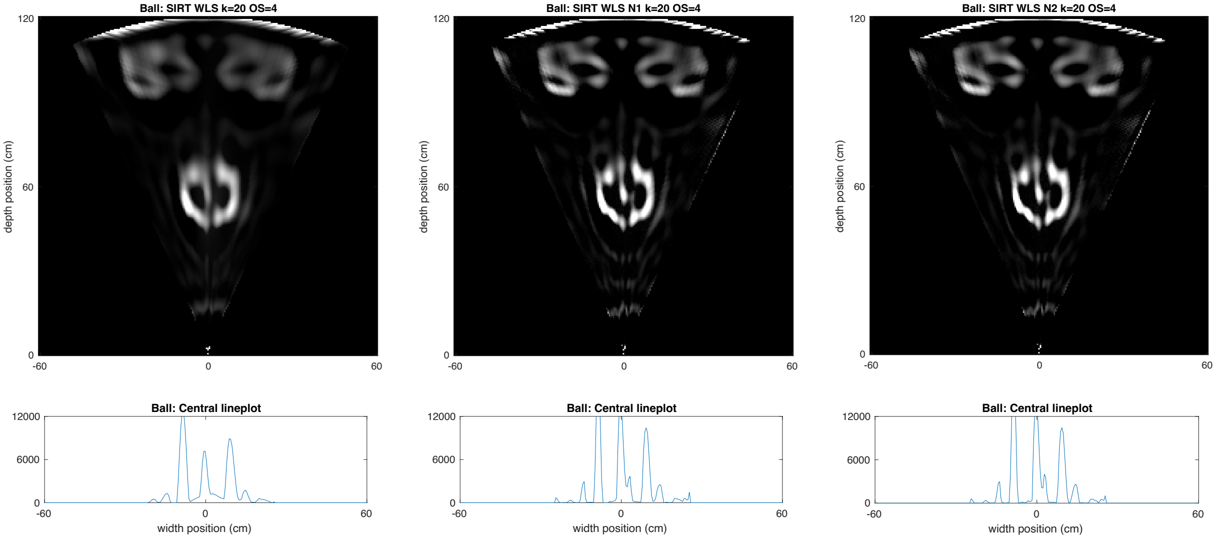

Figure 2. Reconstruction of DU cylinder and ball after 20 iterations of SIRT WLS + N1 and N2 for OS=4.

Table 1 lists TV values for the images produced after 20 iterations. Higher values result for larger OS values and when using N1 and N2 accelerations. These values indicate that sharper images were produced. Table 1 also lists elapsed times for OS = 4 when using a 2019 quad-core MacBook Pro (2.8 GHz Intel iCore 7) vs. a 2021 10-core MacBook Pro (3.2 Ghz Apple M1 Pro). The old computer took 2.5 min to produce an image, but the new computer produces an image in a little more than 30 s. **Thus a volumetric image can be reconstructed in less than 1 min using readily available commodity hardware.**

Table 1. Computational statistics

	TV($\boldsymbol{x}$)			**Elapsed time (s)**	
	OS = 1	**OS = 2**	**OS = 4**	**Mac iCore7**	**Mac M1 Pro**
SIRT WLS	1.49×10^8	1.88×10^8	2.39×10^8	140.1	33.2
SIRT WLS N1	1.75×10^8	2.68×10^8	5.19×10^8	144.4	30.2
SIRT WLS N2	2.06×10^8	2.81×10^8	5.41×10^8	146.2	33.8

2.2.2 Imaging Geometry Update

The imaging geometry was changed to reflect the change to the use of a flat panel pixelated detector placed directly behind the object and an alpha-particle detector with double the number of alpha pixels (details of the panel are described elsewhere [15]). The code was modified to simultaneously support the two geometries.

2.2.3 Timing Calibration

A potential cause of the jagged, noncircular appearance of the cylinder in Figure 2 is imperfect timing calibration of the detector system used to record projection data. To evaluate this possibility, the code was updated to facilitate forward projection of simple geometric objects, including a point, a slab, and a cylinder. Reconstructing the idealized forward-projected data produced artifact-free images. Randomizing the number of neutrons emitted along an alpha ray had no visible effect. However, randomizing the timing associated with an alpha ray led to jagged-looking objects. A correction algorithm was developed based on measurement of the slab geometry. In the algorithm, the reconstructed intensity weighted average is compared with the least squares fit for the slab. The difference is converted to time shifts in the alpha ray directions, which subsequently are used to offset the projection data. The process is repeated until convergence or for a fixed number of iterations. To avoid introducing a bias, the average total is subtracted from each offset. This work is in progress. Figure 3 illustrates the problem and the envisioned solution for uniformly distributed random offsets in the range of ±0.25 ns. Figure 4 likewise shows the results for normally distributed zero-mean random offsets with a standard deviation of 0.25 ns. Each alpha ray was given its own offset in both cases. The left images show the reconstruction result when timing offsets are not considered. The middle images show the results of knowing the offsets. The right images show the results of applying the correction algorithm. The jaggedness is gone when the offsets are known and are visibly reduced when corrected for, more so for the uniform offsets than the normally distributed offsets that cover a wider range. The results were derived from forward-projected data using the new flat-panel geometry for a small number of large detector pixels. Reconstruction was based on 20 iterations of SIRT WLS N2 using OS = 4. The circumstances under which the needed corrections can be achieved are being investigated.

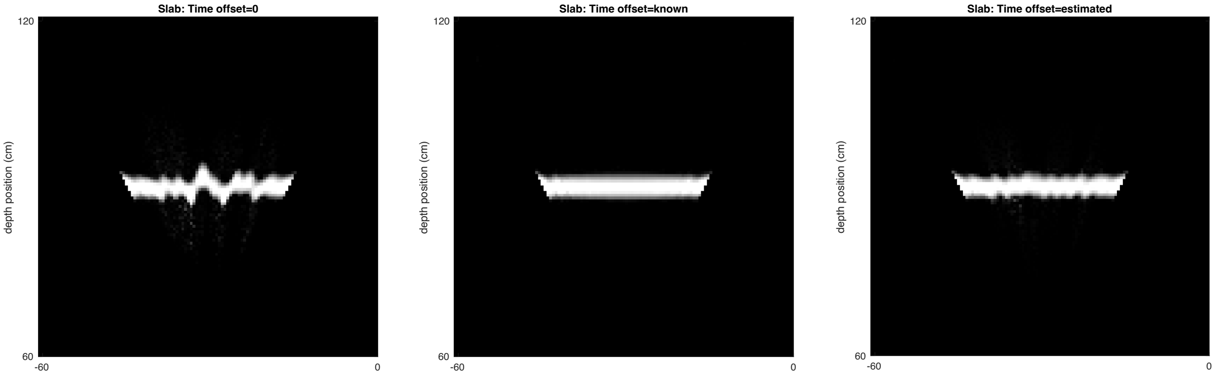

Figure 3. Slab reconstructions for uniformly distributed timing offset estimates.

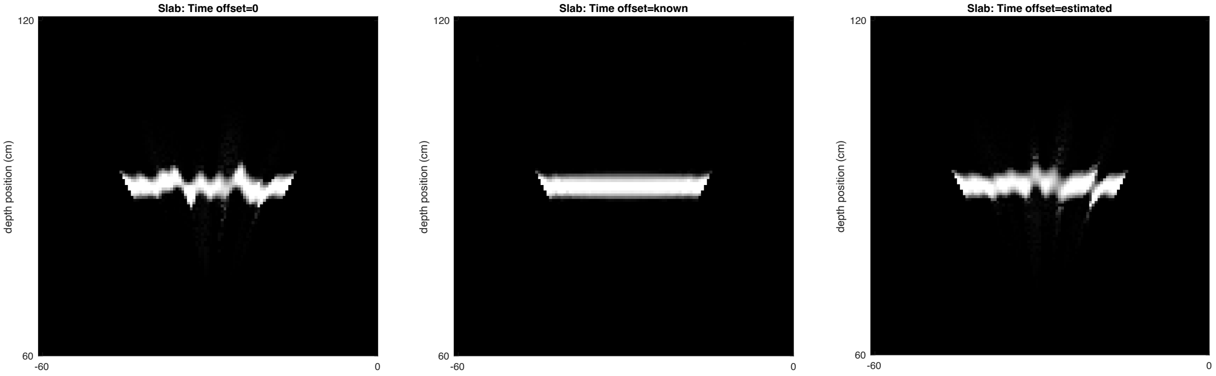

Figure 4. Slab reconstructions for normally distributed timing offsets.

3. DECOMPOSITION OF X-RAY AND NEUTRON RADIOGRAPHY INTO A MATERIALS BASIS

Pacific Northwest National Laboratory previously developed a method to perform quantitative material reconstructions using radiography data for x-rays [16] and for x-rays and neutrons [17]. In this methodology, each pixel of the transmission image is decomposed into the optimal quantities of basis materials, in which the number of basis materials equals the number of distinct interrogations. This method requires an accurate understanding of the radiography system response and combines a physics-informed calculation of the expected response with inverse methods to quantitatively reconstruct the areal densities of a short list of known materials for the inspected object. The method also requires appropriate basis materials to be known.

Recent interest in using neutron radiography to noninvasively interrogate objects provided an opportunity to adapt this algorithm to combined neutron and x-ray radiography data. Data acquired using API systems are not only of particular interest because the API method enables reduced neutron scattering on the imaging plane for transmission measurements but also because observation of additional induced-reaction signatures, such as secondary gamma emission and neutron scattering, allow new forms of contrast [18–20]. The inverse problem framework is flexible to adding other observables from the API system to produce high-accuracy material reconstructions.

3.1 HIGH-LEVEL SUMMARY OF FY 2020 and FY 2021

A summary of progress for FY 2020 and FY 2021 can be found in previously published reports [1,2].

3.2 SUMMARY OF FY-2022 PROGRESS

In FY 2022, Pacific Northwest National Laboratory tested and extended the material estimation algorithm to operate on experimental data using neutron radiography as well as mid- and high-energy x-ray radiography data. The material estimation algorithm estimates material thickness based on a physical model of the interrogation system, including a model of the source energy spectrum, the transmission of neutrons and x-rays through an object, and the detection of the neutrons and x-rays on a radiographic detector. FY 2021 finished with a measurement campaign performing radiography of many items using D-T (14 MeV) neutrons and mid-energy (<350 keV) x-rays. Progress was made in FY 2022 on modeling those radiography systems and understanding the complexity of accurately modeling both modes of a dual-mode system. However, the data were limited by the limited transmission of the mid-energy x-ray data.

A second measurement campaign was performed in FY 2022 using high-energy x-rays with energy up to 7.5 MeV. These x-rays are more penetrating than the mid-energy x-rays, enabling high-quality and low-noise x-ray radiographs to be acquired. DT neutron radiography data with the API neutron system were also acquired of the same set of items. These image data can be registered and analyzed in the material estimation algorithm to make accurate material thickness estimations from x-ray and neutron radiography data.

The physics model used in the material estimation algorithm has been updated to accurately represent the high-energy x-ray and neutron radiography systems. This update includes an accurate model of object scatter, source energy spectrum, and detector response. Initial results with the new data are encouraging, but errors in the material thickness estimations indicate that more work is needed to update and refine the physics model to enable accurate material thickness estimations.

3.3 MATERIAL ESTIMATION THEORY

As in previous work [17], quantitative material reconstructions are created using a physical model of the interrogation system. The baseline model describes how a set of material thicknesses attenuates a beam of x-rays or neutrons as it passes through an object to a radiographic detector pixel.

A detector response model r_{ijk} for a given pixel ij and interrogating particle k is defined as

$$r_{ijk}(\vec{\rho}_{ij}) = \int_E \varepsilon_k(E)\left[\phi_{0,k}(E)\exp\{-\vec{\mu}(E)\cdot\vec{\rho}_{ij}\} + \phi_{\text{scat}}(E)\right]dE. \tag{1}$$

The detector efficiency is given by ε, and the incident energy-dependent flux is given by ϕ_0. Bremsstrahlung x-ray spectra are assumed, which are broad in energy, in contrast to the nearly monoenergetic neutron spectrum from a D-T neutron generator. The attenuation coefficient for x-ray or neutrons is given by μ, and the material thicknesses in pixel ij, as areal densities, are given in the material vector $\vec{\rho}_{ij}$, denoting that multiple materials may be present in the beam path (here, the dot product simply denotes that the attenuation coefficient for each material only operates and the areal density of that material). The scattered flux incident on the image plane, from the object or the surroundings, is given by ϕ_{scat}.

Scatter estimation is expanded from that detailed in previous work [21]. Whereas previous work used Monte Carlo N-Particle (MCNP) simulations to estimate scatter kernels, the method is here extended to determine scatter kernels from experimental data of object slabs. Because scatter is material dependent, a scatter kernel function for x-rays and neutrons is fitted to the observed object slab radiographs of polyethylene and aluminum.

As is typical with radiographic analysis, to remove detector efficiency and image brightness inhomogeneities, the measured pixel response with the object in place $r_{ijk}(\vec{\rho}_{ij})$ is divided by that without the object in place $r_{ijk}(\vec{0}_{ij})$:

$$d_{ijk} = \frac{r_{ijk}(\vec{\rho}_{ij})}{r_{ijk}(\vec{0}_{ij})}, \tag{2}$$

where $\vec{0}_{ij}$ denotes that the thickness vector is set to zeros.

The inverse problem is posed as a least-squares fit of the data model vector $\vec{d}(\vec{\rho})$ for all pixels and radiographs to the equivalent observed data vector d_{obs} with total-variation regularization, *TV*:

$$\min_{\vec{\rho}} \frac{1}{2}\left\|\vec{d}_{\vec{\rho}} - \vec{d}_{\text{obs}}\right\|^2 + \alpha TV(\vec{\rho}), \tag{3}$$

The optimization problem is to find the best set of material areal densities that fit the observed data. Total variation regularization *TV* is added to the inverse problem to stabilize solutions that can be sensitive to noise. The present analysis does not use regularization: $\alpha = 0$. For each reconstruction, a set of materials is selected, and the thickness is reconstructed for each material in the set.

3.3.1 X-Ray Scatter Correction Theory

As previously shown [21,2], the scatter estimation methods of Ohnesorge, T. Flohr, and K. Klingenbck-Regn [22] can be adapted for use in material estimation. However, that work assumed that all matter in the radiograph scattered the same way. Different scattering behavior is expected for different materials, particularly between high atomic number (*Z*) and low-*Z* materials. The following treatment incorporates multiple materials with different scattering properties into the scatter estimation. The notation used in this section is given in Table 2.

Table 2. Symbols used in the scatter correction equations

Symbol	Meaning
$I(\boldsymbol{r})$	Observed signal
$I_T(\boldsymbol{r})$	Transmitted signal
$I_S(\boldsymbol{r})$	Scattered signal
$I_f(\boldsymbol{r})$	Forward scatter signal
$I_0(\boldsymbol{r})$	Noninteracting signal
$\boldsymbol{r}$	Detector pixel
x	Distance from source
l	Farthest distance from source of object
$\mu(x,\boldsymbol{r})$	Attenuation coefficient of material
K_f	Forward scatter fraction of material
$\alpha(\boldsymbol{r})$	Attenuation lengths through material

The x-ray removal method assumes a pencil x-ray beam is heading toward the detector at $\boldsymbol{r}$. It encounters object 1 made of a material with attenuation coefficient $\mu_1(x,\boldsymbol{r})$ and forward scatter fraction K_{f1}starting at a distance $x = 0$ and continuing to $x = l_1$. It then passes to object 2 with attenuation coefficient $\mu_2(x,\boldsymbol{r})$ and forward scatter fraction K_{f2} at $l_1 < x < l_2$. Each of these objects has its own attenuation length:

$$\alpha_1(\boldsymbol{r}) = -\textstyle\int_0^l dx\ \mu_1(x,\boldsymbol{r}) \tag{4}$$

$$\alpha_2(\boldsymbol{r}) = -\int_0^l dx\ \mu_2(x,\boldsymbol{r})$$

Within object 1, the transmitted intensity at any point x is

$$I_{T1}(\boldsymbol{r}) = I_0(\boldsymbol{r}) \exp\left\{-\int_0^x dx'\ \mu_1(x',\boldsymbol{r})\right\}\ , \tag{5}$$

and in object 2, the transmitted intensity at any point x is

$$I_{T2}(\boldsymbol{r}) = I_0(\boldsymbol{r}) \exp\left\{-\int_0^x dx'\ \mu_2(x',\boldsymbol{r})\right\}\ \exp\{-\alpha_1(\boldsymbol{r})\}\ . \tag{6}$$

The rate of change of the transmitted signal in material m is

$$\frac{dI_{Tm}(x,\boldsymbol{r})}{dx} = -\mu_m(x,\boldsymbol{r})\ I_{Tm}(x,\boldsymbol{r}), \tag{7}$$

and the intensity of scattering in the forward direction is

$$\frac{dI_{fm}^{(0)}(x,\boldsymbol{r})}{dx} = K_{fm}\ \mu_m(x,\boldsymbol{r})\ I_{Tm}(x,\boldsymbol{r}). \tag{8}$$

The amount of forward scattering reaching the detector is

$$\frac{dI_{f1}(x,\boldsymbol{r})}{dx} = K_{f1}\,\mu_1(x,\boldsymbol{r})\,I_{T1}(x,\boldsymbol{r})\;\exp\left\{-\int_x^{l_1} dx'\;\mu_1(x',\boldsymbol{r})\right\}\;\exp\{-\alpha_2(\boldsymbol{r})\} \tag{9}$$

$$= K_{f1}\,\mu_1(x,\boldsymbol{r})\,I_0(\boldsymbol{r})\;\exp\{-\alpha_1(\boldsymbol{r})\}\;\exp\{-\alpha_2(\boldsymbol{r})\}\; = K_{f1}\,\mu_1(x,\boldsymbol{r})\,I_T(\boldsymbol{r}),$$

$$\frac{dI_{f2}(x,\boldsymbol{r})}{dx} = K_{f2}\,\mu_2(x,\boldsymbol{r})\,I_{T2}(x,\boldsymbol{r})\;\exp\left\{-\int_x^{l_2} dx'\;\mu_2(x',\boldsymbol{r})\right\}$$

$$= K_{f2}\,\mu_2(x,\boldsymbol{r})\,I_0(\boldsymbol{r})\;\exp\{-\alpha_1(\boldsymbol{r})\}\;\exp\{-\alpha_2(\boldsymbol{r})\}\; = K_{f2}\,\mu_2(x,\boldsymbol{r})\,I_T(\boldsymbol{r}).$$

Integrating over x yields

$$I_{f1}(x,\boldsymbol{r}) = K_{f1}\,\alpha_1(x,\boldsymbol{r})\,I_T(\boldsymbol{r}), \tag{10}$$

$$I_{f2}(x,\boldsymbol{r}) = K_{f2}\,\alpha_2(x,\boldsymbol{r})\,I_T(\boldsymbol{r}).$$

Each material has its own angular scattering distribution, and thus its own scatter kernel $U_m(\boldsymbol{r})$. Thus, the total scatter signal is

$$I_S(\boldsymbol{r}) = \int d^2r'\;I_{f1}(\boldsymbol{r}')\,U_1(\boldsymbol{r}-\boldsymbol{r}') + \int d^2r'\;I_{f2}(\boldsymbol{r}')\,U_2(\boldsymbol{r}-\boldsymbol{r}'). \tag{11}$$

For three or more scattering materials, the math is the same, and the process generalizes in the obvious way:

$$I_{fm}(x,\boldsymbol{r}) = K_{fm}\,\alpha_m(x,\boldsymbol{r})\,I_T(\boldsymbol{r}), \tag{12}$$

$$I_S(\boldsymbol{r}) = \sum_m \int d^2r'\;I_{fm}(\boldsymbol{r}')\,U_m(\boldsymbol{r}-\boldsymbol{r}').$$

An algorithm can now be developed to estimate the scatter in an image:

1. Obtain an estimate of K_{fm} and $U_m(\boldsymbol{r})$ for all materials of interest.
2. Approximate $I_T(\boldsymbol{r}) = I(\boldsymbol{r})$.
3. Estimate the material composition.
4. Estimate the scatter $I_S(\boldsymbol{r})$ using the method outlined above.
5. Find a better approximation of the transmission $I_T(\boldsymbol{r}) = I(\boldsymbol{r}) - I_S(\boldsymbol{r})$.
6. Iterate using this method until $I_T(\boldsymbol{r})$ converges.

Section 3.5.2.2 discusses a method used to obtain K_{fm} and $U_m(\boldsymbol{r})$ for different materials.

3.3.2 Interrogation System Modeling

Accuracy in the material estimation algorithm is directly affected by accuracy of the physics (forward) model that is being used to complete the inverse problem of determining material thicknesses. Other than object scatter, having an accurate understanding of the incident x-ray spectrum and detector response is particularly important.

The incident x-ray spectrum was modeled using MCNP6 [23] for a pencil beam of electrons of given energy impinging on a tungsten target. MCNP calculates the radiation that is emitted from the electrons as they are decelerated in the tungsten target to simulate x-ray generation in a high-energy bremsstrahlung x-ray source such as a betatron. Example results from these simulations are shown in Figure 5. The calculated spectra provide the initial model for the incident x-ray spectra ϕ_0 in Eq. (1).

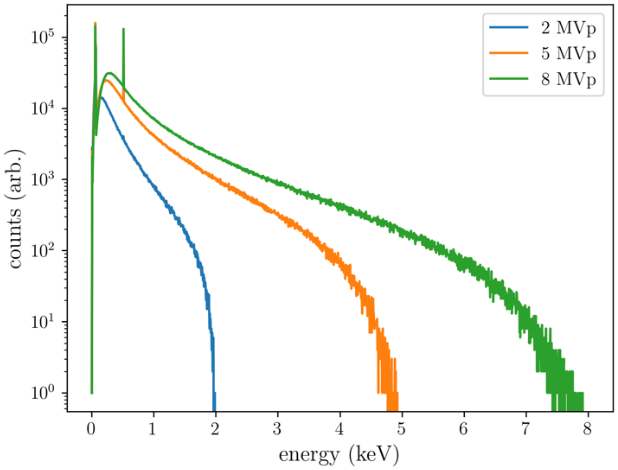

Figure 5. Modeled bremsstrahlung x-ray spectra to simulate the spectrum that is coming from the high-energy betatron x-ray source.

A model of the x-ray system detector response was also developed using MCNP radiation transport simulations. The detector used in all acquisitions of x-ray radiographs was the Varex 4343HE. The detector has a gadolinium oxysulfide scintillator combined with a 1 mm thick copper conversion later to increase its efficiency for high-energy x-ray radiography. Because the scintillator on its own is relatively low efficiency, <1%, for x-rays having energies greater than 2 MeV, the copper conversion layer is placed in front of the scintillator to reduce the energy of the incident beam and increase detector efficiency. This feature is unique to the digital x-ray panels built by Varex compared with other manufacturers, such as Novo.

An MCNP model of this system was made consisting of a monodirectional beam of x-rays impinging on a 1 mm thick copper layer and then the scintillator. Radiation transport simulations were performed to determine energy deposition in the scintillator material as a function of incident energy. The result of this calculation is shown in Figure 6: the efficiency with respect to incident x-ray energy is plotted with and without the 1 mm copper conversion layer. Although the copper layer reduces efficiency at low energies (<200 keV) owing to attenuation in the copper, it considerably increases efficiency for high-energy x-rays, increasing it by 20%–40% at energies greater than 6 MeV.

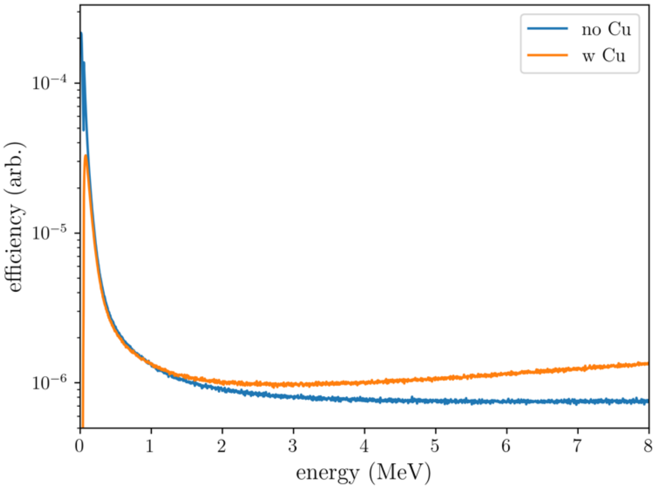

Figure 6. An MCNP model of the Varex x-ray radiography detector efficiency with and without a 1 mm layer of copper in front of the scintillator to increase efficiency at higher energies.

The model for the neutron API system does not require the sane fidelity as the x-ray model in the energy response of the system. Since the neutron API system is largely monoenergetic at 14 MeV, the detector efficiency as a function of energy does not need to be accounted for. This is a particular benefit for making quantitative measurements from the neutron radiography system. Also, the neutron API data can be processed to remove much of the scattered radiation. Though the neutron estimation algorithm will likely need better scatter estimates than are currently used, scatter in the x-ray data will cause greater errors and so the study of the neutron scatter and how it affects the results is left for a later time.

3.4 EXPERIMENTAL DUAL X-RAY/NEUTRON RADIOGRAPHY DATA

Two experiments were performed in which x-ray and neutron radiography data were recorded and the images registered for processing in the reconstruction algorithm. The first experiment used mid-energy x-rays (<400 keV), whereas the second used high-energy x-rays (in the megaelectronvolt range). The mid-energy x-rays were produced by a Golden Engineering XRS4 portable x-ray generator, which produces bremsstrahlung x-rays with a maximum energy of 370 keV. X-ray radiographs were recorded by the Varex 4343HE, which has a gadolinium oxysulfide scintillator, an active area of 42.7 × 42.7 cm, and 139 μm^2 pixel pitch. The neutron radiography system used a Thermo Fisher Scientific API120 D-T neutron source to produce 14.1 MeV neutrons. The neutron detector consisted of a custom 30 × 30 pixel array with 1.04 × 1.04 × 5.0 cm pixels of organic scintillator EJ-299-33M [15]. Each 5 × 5 group of pixels is optically coupled to a Hamamatsu H12700 position-sensitive photomultiplier tube (PMT), and the position of a neutron interaction within in a quadrant of nine such photomultiplier tubes is determined with Anger logic. The x-ray data is registered and downscaled to match the neutron data. The experimental setup is pictured in Figure 7.

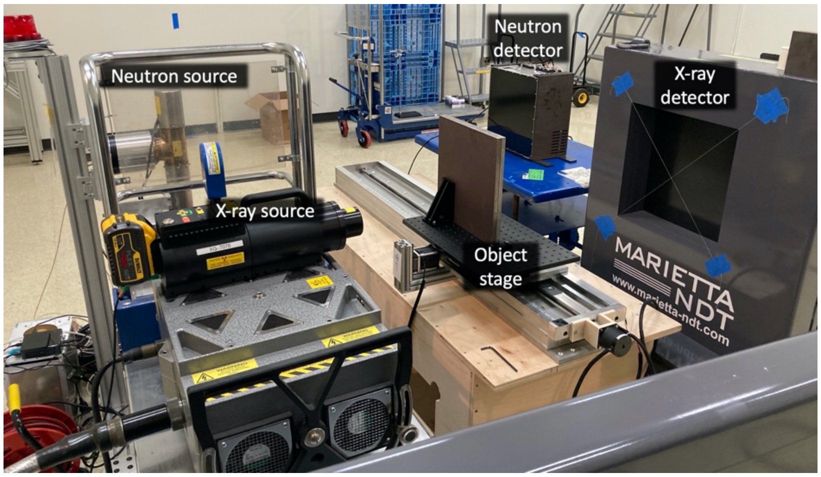

Figure 7. The dual-mode experimental setup showing the x-ray and neutron radiography systems with a stage to move interrogated objects between the two systems.

The maximum x-ray energy of 370 keV resulted in limited transmission through many objects that were interrogated. Therefore, a second experimental campaign was performed that used a JME PXB7.5M Betatron x-ray source with energies up to 7.5 MeV. These energies are much more penetrating and allow interrogation of substantially larger, denser objects. The same neutron source was used for this campaign as that previously used.

Several objects were interrogated as part of the high-energy x-ray and neutron radiography measurement campaign, including material blocks that were used to quantify material scatter and annuli and concentric shells that enabled simultaneous measurement of a range of material thicknesses to test the material reconstruction algorithms. X-ray radiographs were generated using the high-energy betatron at endpoint energies of 4 MeV and 7.5 MeV, and a neutron radiograph was generated with the API neutron imager. An example object consisting of aluminum and copper concentric shells and its associated radiographs are shown in Figure 8 and Figure 9.

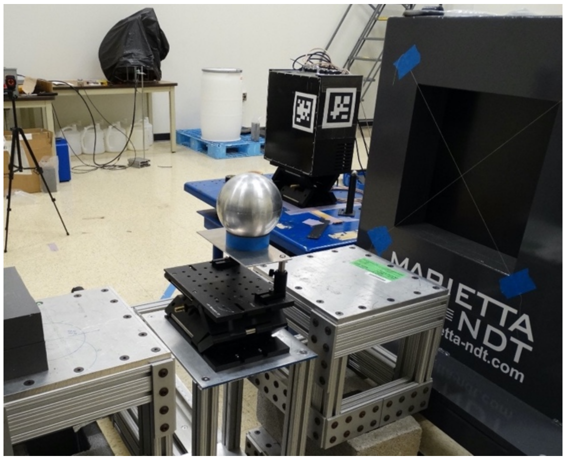

Figure 8. The concentric shell object comprises aluminum and copper shells with ODs of 5 and 4 in., respectively.

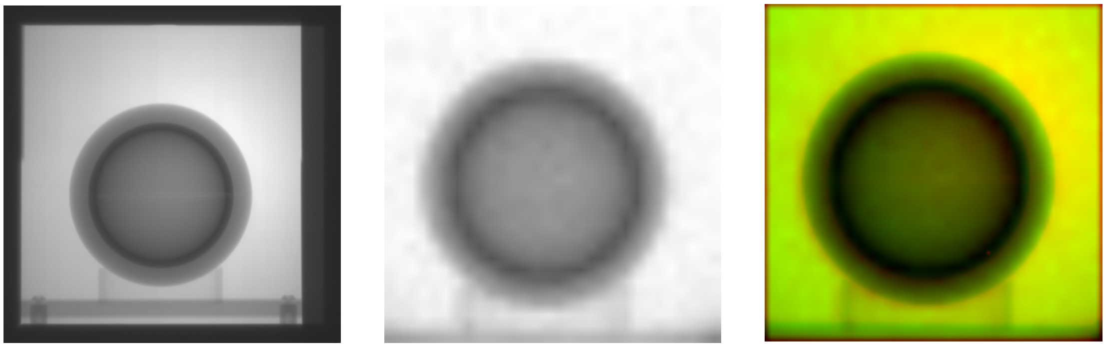

Figure 9. Images of the concentric shells object. (*left*) X-ray and (*center*) neutron radiographs of the concentric shells object. (*right*) An overlay of the registration of the x-ray and neutron images. Here, the x-ray radiograph is downscaled to the 30 × 30 pixel array that the neutron API radiography data are on.

3.4.1 Experimental Design

Modeling studies were used to select the x-ray endpoint energies and filtration that would maximize the ability to perform quantitative material estimations. The Cramer–Rao Lower Bound (CRLB) was used to explore this ability [24]. The CRLB represents the lower limit of the uncertainty that would be expected from an unbiased estimator, such as one determined from a least-squares misfit. Here, material thicknesses are the estimated parameters. The CRLB for material *p*, σ_ρ, is calculated using first derivatives of the forward model, Eq. (1).

$$\sigma^2_{\rho_p} \geq F^{-1}_{pp}, \tag{13}$$

$$\text{where } F_{pq} = \sum_k \frac{1}{\sigma_r^2} \frac{\partial r_{ijk}(\vec{\rho})}{\partial \rho_p} \frac{\partial r_{ijk}(\vec{\rho})}{\partial \rho_q}.$$

Here F^{-1} is the inverse of the Fischer information matrix, where the *pp* subscript denotes the diagonal of F at the *p*th location. The sum is over all the inspections *k* used in the analysis. The variance of the measurement is given by σ_r^2.

The CRLB signal-to-noise ratio (SNR_{crlb}), is used to optimize the endpoints and x-ray filtration used to interrogate an object. The CRLB SNR is defined as the ratio of the quantity of the parameter being estimated, here material thickness ρ, to the CRLB value for the parameter σ_{ρ_p}:

$$SNR_{\text{crlb}} = \frac{\rho}{\sigma_{\rho_p}}. \tag{14}$$

Using the SNR_{crlb} measure, optimal beam endpoints and filtration can be selected from those available. Figure 10 shows the result from one calculation, here optimizing for estimation of a thickness of 10 cm of stainless steel and 10 cm of DU. The SNR_{crlb} measure is shown for all possible x-ray potentials between 2 and 8 megavolt peak (MVp) and lead filters between 0 and 10 cm. From left to right, lower SNR is observed for endpoints that are close to one another because the spectra are largely overlapping. An optimal set of two endpoints and filtration is found to be 4 and 8 MVp with a 0.5 in. lead filter. This set was the basis for choosing the endpoints and filtration used in the measurement campaign using high-energy x-ray radiography.

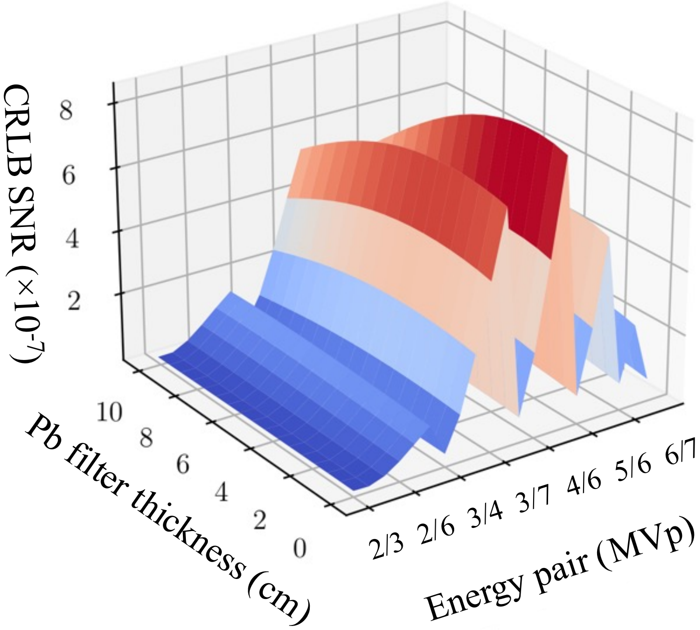

Figure 10. The CRLB SNR measure for estimating thicknesses of polyethylene and stainless steel. The CRLB SNR measure is shown for a variety of x-ray endpoint pairs and lead filter thicknesses. The best SNR is achieved for the pair of energies of 4 and 8 MVp and a filter thickness of 1.2 cm.

3.5 MATERIAL ESTIMATION USING NEUTRON AND X-RAY RADIOGRAPHY

3.5.1 Neutron and Low-Energy X-Ray Radiography Data

Two objects were used to evaluate performance of the neutron and low-energy x-ray radiography system: slabs of polyethylene and aluminum. The registered x-ray and neutron radiographs were processed by optimizing Eq. (3). Depending on the object being interrogated, a two-material set is supplied to the algorithm. For the 5.08 cm thick polyethylene (poly) slab data, the material set is {poly, steel}. For the 1.27 cm thick aluminum slab data, the material set is {Al, steel}. The results indicate the ability to estimate the slab thickness and bound the possibility for confusion between the slab material and steel. Material confusion is an indication of errors in the physics model, Eq. (1).

An example of the output from the algorithm is shown in Figure 11, which shows materials estimated at each pixel. Results are summarized in Table 3. Assuming material densities of 0.93 g/cm^3 for poly and 2.7 g/cm^3 for aluminum, material thicknesses estimated are within 10% of the actual. This performance is good, but it indicates that a higher-fidelity physics model should be developed. One such improvement could be an update to the x-ray detector efficiency model.

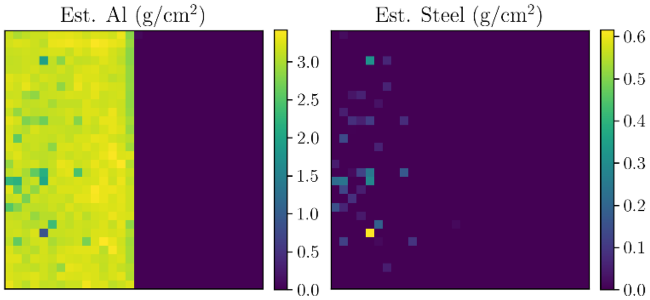

Figure 11. Material estimations for the aluminum slab data. The estimations are made from registered radiographs from the x-ray and neutron system. The x-ray data were downbinned to match the pixel size for the neutron data.

Table 3. Material reconstruction accuracy for the material slab data

Object	Actual thickness (cm)	Estimated thickness (cm)	Error
Poly slab	5.08	5.51	+8.4%
Al slab	1.27	1.15	−9.1%

Note: Values reported here are averaged over the regions where the material slab resides.

3.5.2 Neutron and High-Energy X-Ray Radiography Data

3.5.2.1 Deblurring

Initial review of the high-energy x-ray radiography data revealed unexpected properties. Previous investigations used regions of elevated counts adjacent to the radiographed object to fit a point scatter function for scatter estimation. Physically, this behavior is expected as x-rays incident on the object scatter out of the object’s shadow. If scattering is more likely at smaller angles and falls off with distance from the scattering source, then it would result in increased intensity close to the object’s x-ray shadow that falls off to background levels far from the object’s shadow. However, many of the objects from this set of measurements showed the opposite behavior: the intensity adjacent to the shadow was below background, and no areas were above background. This analysis is shown for radiographs of lead and aluminum in Figure 12, Figure 13, and Figure 14.

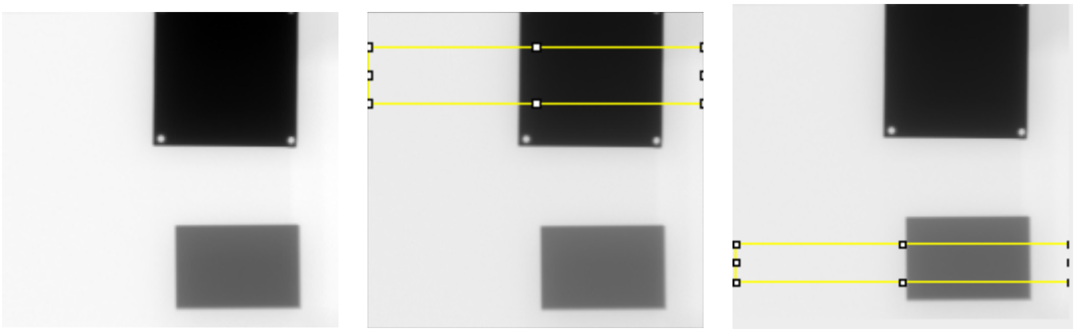

Figure 12. A radiograph of a 1 in. thick aluminum (bottom row) and 0.25 in. thick lead (top row) block with a 4 MV betatron spectrum, after dark field and flat field corrections. (*left*) Bare image. (*center*) The image with a region selected across the lead block for a brightness profile. (*right*) The region selected across the aluminum block for taking brightness profiles.

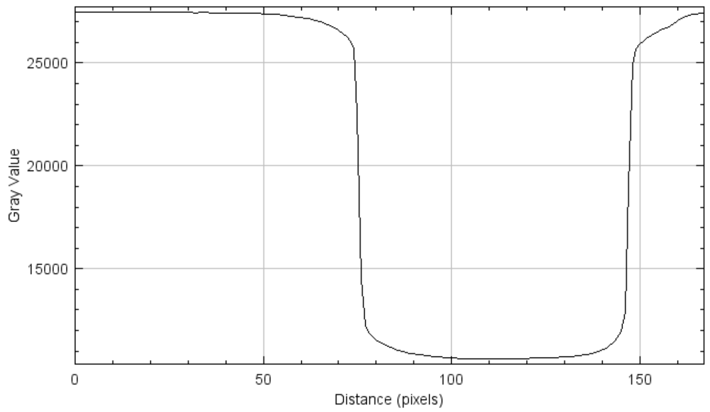

Figure 13. The brightness profile across the lead block selection shown in Figure 12. The pixel axis was downbinned by 16.

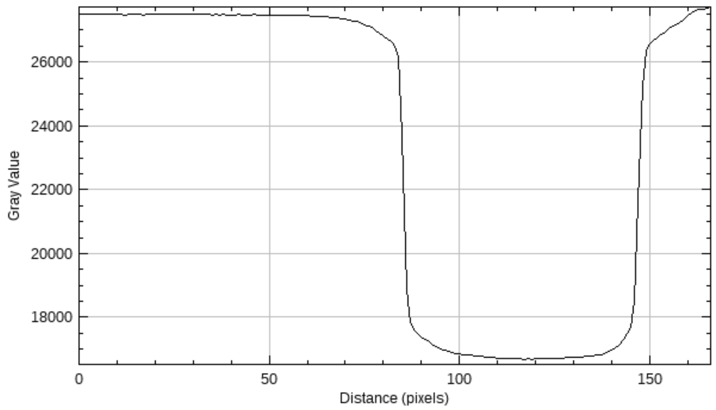

Figure 14. The brightness profile across the aluminum block selection shown in Figure 12. The pixel axis was downbinned by 16.

The most likely explanation is that this behavior is caused by detector blurring, possibly a result of using the conversion screen that increases sensitivity at higher photon energies but which, because of its offset from the detector, could lead to a spreading of the converted signal. To correct this blurring, we developed a blind deconvolution algorithm, assuming a point spread function (PSF) of the form

$$PSF(r) = W_0\, \delta(r) + \sum_{i=1}^{N} \frac{W_i}{2\,\pi\,\sigma_i^2} \exp\left\{-\frac{r^2}{2\,\sigma_i^2}\right\}, \tag{15}$$

where $N = 3$. This PSF is normalized, with an enforced

$$\sum_{i=0}^{N} W_i = 1. \tag{16}$$

In the absence of noise, it is assumed that the area outside the object shadows should reach a constant background value, and the area inside the shadow of a uniform slab should reach a constant value because of uniform absorption. The boundary region between the inside and outside of the shadow, or regions of nonconstant thickness, was not further constrained.

A Wiener deconvolution with the PSF on the measured image was used to generate a deconvolved image $D(\boldsymbol{r})$. The goodness of the PSF and the assumed constant values can be estimated with a χ^2 value.

For each pixel $\boldsymbol{r}$:

- If the pixel is in a region of fixed value V, then add $\left(V - D(\boldsymbol{r})\right)^2$ to χ^2.
- Otherwise, if $D(\boldsymbol{r}) < 0$, then add $\left(D(\boldsymbol{r})\right)^2$ to χ^2.
- Otherwise, do not change χ^2 for this pixel.

A direction set minimization routine is used to find values of the fit parameters that minimize χ^2, using the weights of the PSF basis functions, the widths of the Gaussian basis functions, and the constant values of the interior regions as the values that were fit.

The high-energy x-ray data largely consisted of images collected using two spectra: 4 MVp with no filter and 7.5 MVp with a 0.5 in. lead filter. These spectra introduced different blurring, such that a PSF optimized for one spectrum would not return good results for the other. Consequently, one PSF was fitted for each spectrum. The images used for the fit were those with the lead upper block and aluminum lower block. The image used to fit the 4 MVp spectrum is shown in Figure 12, and the image used to fit the 7.5 MVp filtered spectrum is shown in Figure 15. The fitted parameters for the PSFs are listed in Table 4.

Figure 15. A radiograph of a (*bottom*) 3 in. thick aluminum and (*top*) 0.5 in. thick lead block with a 7.5 MVp betatron spectrum filtered through 0.5 in. lead.

Table 4. Best-fit parameters for the PSFs for the two spectra used

Parameter	4 MVp, no filter	7.5 MVp, 1.27 cm Pb filter
W_0	0.447	0.097
W_1	0.326	0.720
W_2	0.045	0.071
W_3	0.182	0.112
σ_1	0.856	0.505
σ_2	2.856	3.837
σ_3	10.381	12.873

Note: The units of widths are downbinned pixels (pixels/16).

The PSFs showed good results when applied to other images taken with the same spectrum. This is illustrated in Figure 18 and Figure 19, where a radiograph of a set of small blocks taken at 4 MVp is deconvolved with the PSF fitted to the image of Figure 12.

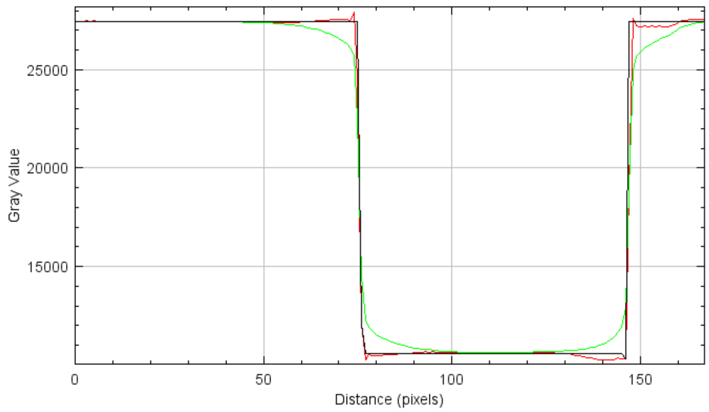

Figure 16. Intensity profiles of the fixed value regions (black), the deconvoluted image (red), and the original blurred image (green) for the profile across the lead block with a 4 MV spectrum. The pixel axis was downbinned by 16.

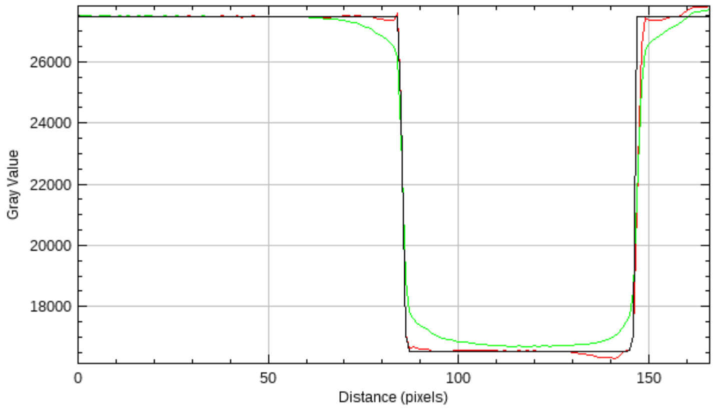

Figure 17. Intensity profiles of the fixed value regions (black), the convoluted image (red), and the original blurred image (green) for the profile across the aluminum block with a 4 MV spectrum. The pixel axis was downbinned by 16.

A similar analysis was performed for a radiograph of ten cubes of different materials shown in Figure 18 and lineout with and without deblurring shown in Figure 19.

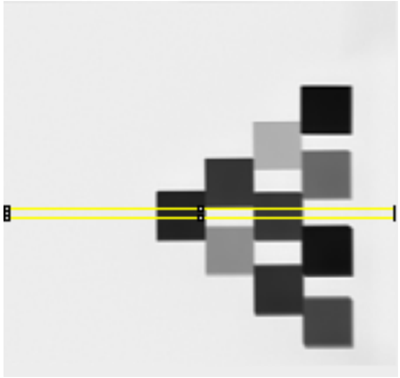

Figure 18. A radiograph of assorted blocks of different materials with a 4 MVp betatron spectrum. The profile section is shown in yellow.

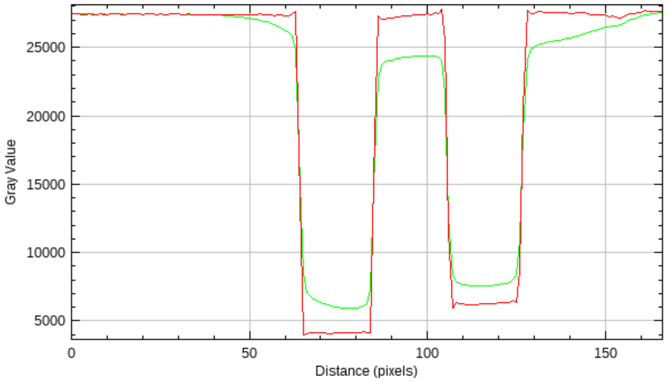

Figure 19. The brightness profile of the block radiograph shown in Figure 18, with the original image profile in green and deconvolved image profile in red, indicating how the deconvolution returned the background regions to a constant value and flattened out the shadows. The pixel axis was downbinned by 16.

3.5.2.2 Descattering

Most of the images taken had no discernable scattering because the scattering was obscured by blurring. However, a set of four images was taken with the object positioned close to the detector to enhance the scattering signal. Figure 20 shows a radiograph of a 5 in. thick polyethylene block placed within approximately 10 cm of the detector screen and illuminated with the 7.5 MVp spectrum filtered through 0.5 in. lead.

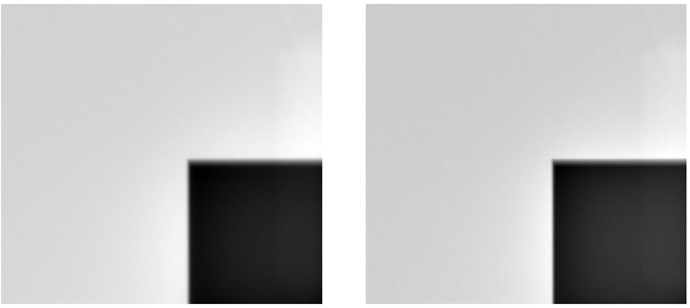

Figure 20. One of the radiographs with evidence of scattering. In this image, a 5 in. polyethylene block was placed within approximately 10 cm of the detector screen and illuminated with the 7.5 MVp spectrum filtered through 0.5 in. lead. The left is as taken; the right is the result of de-blurring. The increase in intensity adjacent to the block’s shadow is visually apparent in this image.

The remaining three images exhibiting scattering included a 3 in. polyethylene block imaged with 4 MVp x-rays, a 0.5 in. steel sheet imaged with 4 MVp x-rays, and a 1.5 in. steel sheet imaged with 7.5 MVp lead filtered x-rays. These other images are visually similar to Figure 20, differing mainly in minor changes to positioning and in the amount of attenuation.

The images were deblurred. Lineouts of the radiograph shown in Figure 20 with and without deblurring are shown in Figure 21.

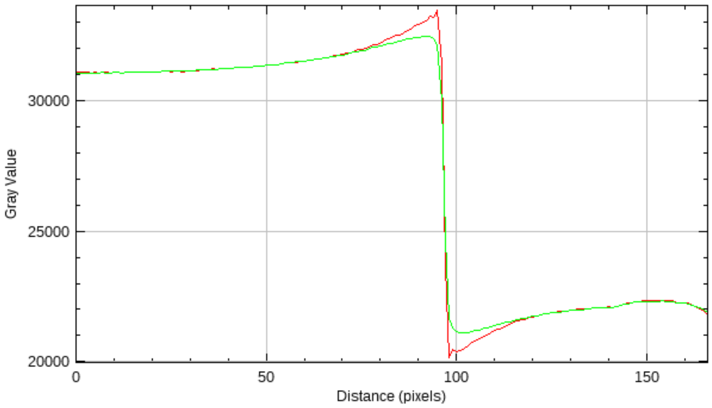

Figure 21. Intensity profile across the polyethylene block of Figure 20 before (green) and after (red) deblurring. The pixel axis was downbinned by 16.

The deblurred images were used as input for the scatter estimation algorithm described in Section 3.3.1. Compared with previous work the project team has done, the large angle fall-off of the wide-angle scatter was neglected as unobservable in the current setup. Additionally, the largely forward-directed coherent scatter would not introduce enough blurring to be distinguishable from a decrease in K, and was thus neglected, leaving a one-parameter fit for the point scatter function:

$$PScF(\theta) = \exp\{-f\theta\}.$$

In previous work, the scatter was estimated from regions with signal higher than background. However, blocks of uniform thickness are expected to exhibit constant transmission. Therefore, signal above the constant transmission signal can also be used to estimate scatter. In a method highly analogous to the deblurring algorithm, the falloff parameter f, forward scatter fraction K, and transmitted values were fitted by minimizing the squared difference between the scatter estimated from the image and the model scatter. This fit resulted in an estimated scatter reduction of between 60% and 70% for the four images.

Table 5. Scatter parameters determined from the polyethylene and steel objects close to the image plane, after the deblurring operation was completed

Object	**3 in. polyethylene**	**0.5 in. steel**	**1.5 in. steel**
Spectrum	**4 MVp**	**4 MVp**	**7.5 MVp—1.27 cm Pb**
K_{scat}	1.256×10^{-6}	8.880×10^{-7}	9.111×10^{-7}
f	2.711	2.491	2.410

Furthermore, the method of interior scatter estimation also applies to objects of known shape, such as spheres, shells, and cylinders. This method is currently implemented for spheres as well as uniform slabs; adjusting the code to handle other shapes should be straightforward. The fitted transmission and scatter for the radiograph of the polyethylene block shown in Figure 20 is shown in Figure 22.

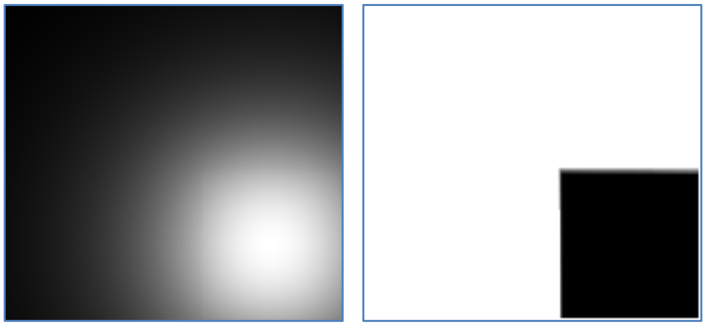

Figure 22. The (*left*) scatter and (*right*) transmitted parts of the signal for the polyethylene block shown in Figure 20.

3.5.2.3 Initial material estimation results

With an accurate initial model of the radiography systems and methods for descattering and deblurring of the radiography data, material estimations can be made from the inverse algorithm, Eq. (3). For this initial look at the results, the polyethylene and steel annulus data are used. Both objects were interrogated with 4 MVp and filtered 7.5 MVp x-ray spectra and 14.1 MeV neutrons. Figure 23 shows the setup of the poly annulus in the x-ray radiography system. The object was also translated on a stage to the neutron API system, and the images were registered as part of data postprocessing. Figure 24 shows x-ray and neutron radiographs of the poly annulus object.

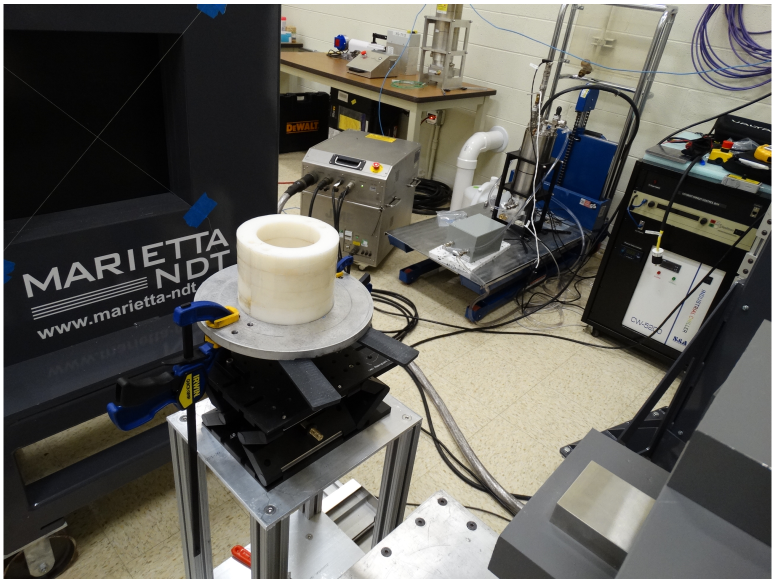

Figure 23. The polyethylene annulus object placed in the x-ray system. The x-ray source is to the lower-right and the detector can be seen in the dark region in the upper-left

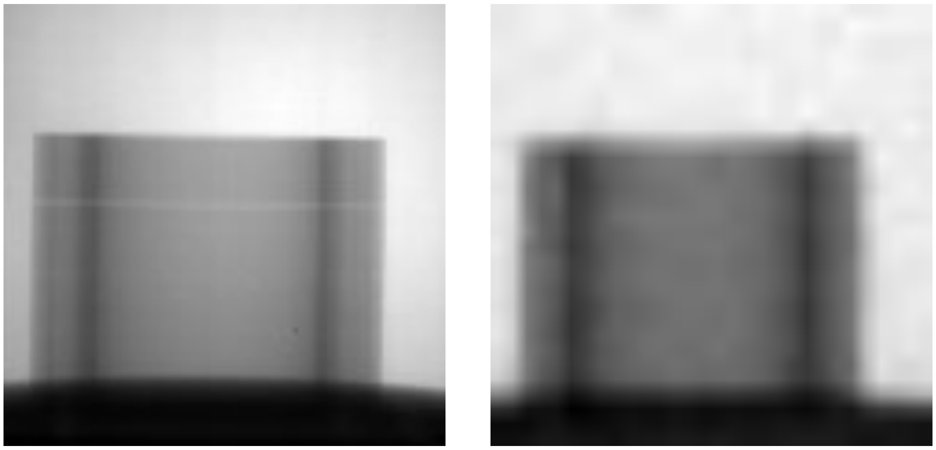

Figure 24. (*left*) X-ray and (*right*) neutron radiographs of the polyethylene annulus object.

Figure 25 shows the material estimation result for the polyethylene and steel annuli. Here, a constant scatter background of 5% of the total signal is assumed. Using the areal density estimated in the center of the object where the thickness of the annuli is 2 in., the algorithm underestimates the thickness by about 10%. Discrimination between poly/steel and DU appears good, as expected because the attenuation coefficients for these materials are sufficiently unique.

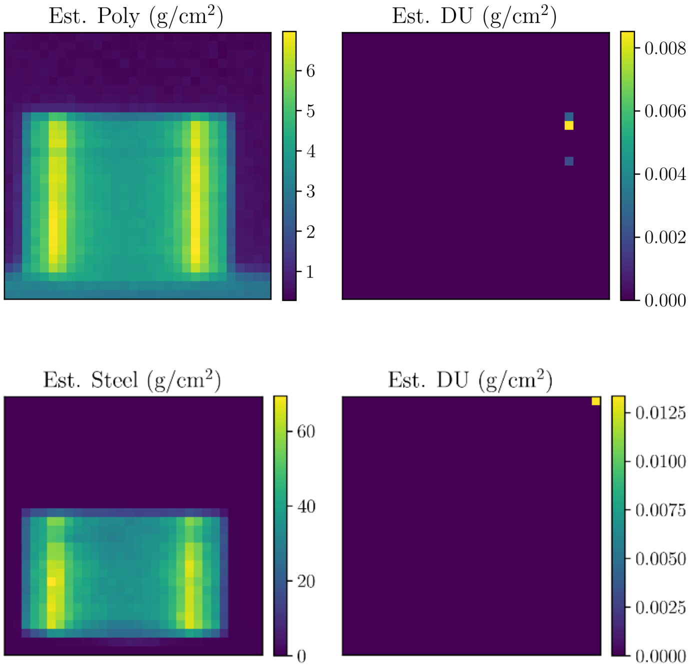

Est. Poly (g/cm^2)

Est. DU (g/cm^2)

Est. Steel (g/cm^2)

Est. DU (g/cm^2)

Figure 25. Material estimations for the (*top*) polyethylene and (*bottom*) steel annulus using the high-energy x-ray and neutron API radiography data.

Figure 26 shows materials estimations using only the x-ray data for the polyethylene. Here, the reconstruction can be performed at a higher spatial resolution (pixel size) because the data do not need to be registered to the low-resolution neutron radiography data. Finer features are more easily viewable with this reconstruction compared with that using the neutron data as well.

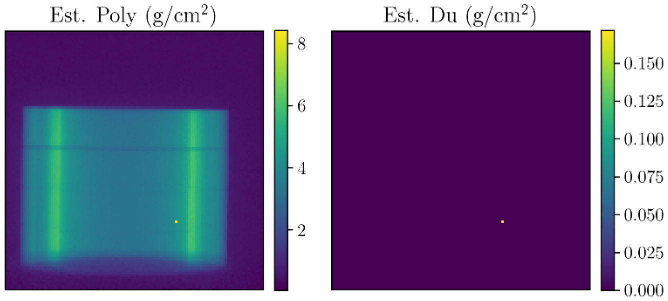

Figure 26. Material estimations using only x-ray data. The data are higher resolution because image registration to the low-resolution neutron radiograph is not required.

Finally, material estimations were performed using the deblurred and descattered data shown in Section 3.5.2. These data had different thicknesses of polyethylene and steel, which were placed near the image plane. Because these data were used to elucidate x-ray scatter, only a single x-ray spectrum was used to interrogate each item. Nonetheless, these single-thickness objects allow a simple check on the performance of the material estimations methods, and errors here are a good indication of errors in the physics model used to make the estimations.

Table 5 summarizes the initial material estimation results. For each of these objects, the estimated thickness is considerably underestimated. Because these data have been deblurred and descattered, scattering is not the most likely cause of the preponderance of the error. The underestimation could be caused by an error in the incident flux spectrum if the spectrum is higher in energy than anticipated in the forward model. In a separate measurement, the betatron spectrum was measured with a $LaBr_3$ detector, so this data will be used to update the model of the incident flux spectrum to reduce these errors.

Table 6. Preliminary material estimation results of material slab data that is placed close to the image plane

Object	Spectrum (MVp)	Actual thickness (cm)	Estimated thickness (cm)	Error
3 in. poly	4	7.62	4.1	−46%
5 in. poly	7.5	12.7	7.5	−41%
1.5 in. steel	7.5	3.81	2.3	−40%

Note: These data have been deblurred and descattered.

3.6 CONCLUSIONS AND OUTLOOK FOR FY 2023

3.6.1 Physics Model

Material estimation results for the low-energy x-ray radiography system and some of the high-energy radiography data indicate material thicknesses that are within about 10% of the actual. This result is encouraging, but more can be done to increase this accuracy, specifically by updating the models for object scatter and the incident x-ray spectrum.

Results from Section 3.5.2.3 indicated that the physics model must be updated to increase accuracy in the material thickness estimations. One clear area where the current model may be inaccurate is the x-ray energy spectrum coming from the betatron. This spectrum was directly observed using a shielded and collimated $LaBr_3$ gamma spectrometer [25]. Analysis of these data is ongoing to properly account for pileup and other effects, but a preliminary spectrum from this analysis is shown in Figure 27. For comparison, the MCNP-calculated spectrum that is currently used by the forward model is also shown and may have significant discrepancies. For example, the 4 MVp spectrum appears to have much higher energies than expected and has a different overall shape. The higher-energy tail is likely due to uncorrected pileup; to analyze the shape, the detector's response must be calculated. However, the overall shape of the spectrum is likely to be sufficiently different to affect the estimated material thicknesses.

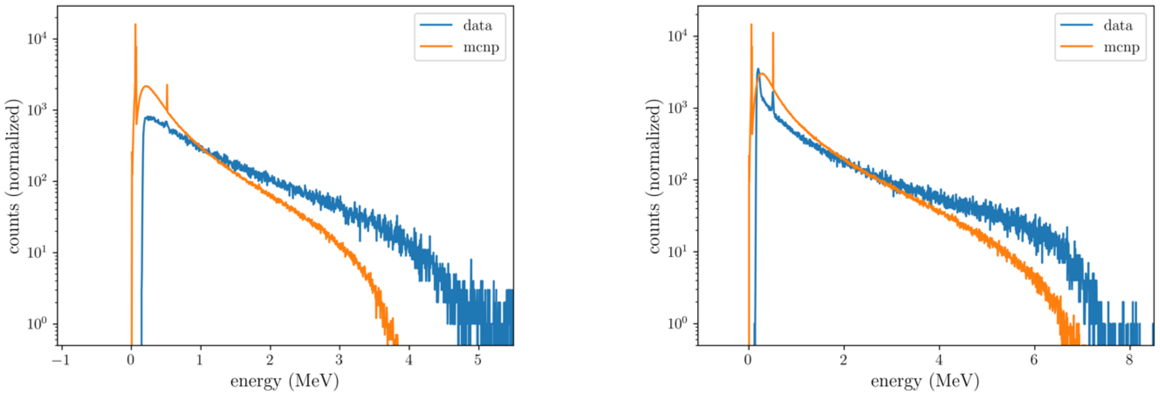

Figure 27. Comparison of the MCNP incident x-ray flux spectrum model assumed in the physics model compared with that observed with a LaBr$_3$ gamma spectrometer.

3.6.2 Descattering and Deblurring

Methods were developed to determine the PSF for image deblurring and the point scatter function for image descattering. Initial results show promise, demonstrating the ability to deblur object edges so they appear sharp and reduce object scatter by 60%–70% in the x-ray radiographs. This investigation will be extended to the other high-energy x-ray and neutron radiography data as the forward model is updated to enable high-accuracy material thickness estimations. As part of future work, the descattering operation could be used in conjunction with the material estimation methods to return path length thicknesses for the materials, which would inform the scatter estimation algorithm by providing mean free path information.

Deblurring was largely material independent for returning the image to sharp edges with flat backgrounds and interiors, as is expected if the blurring were solely a detector resolution issue. If scatter were a significant contributor to the loss of resolution, then different materials with different scatter amounts and distributions would be expected to result in different fitted PSFs for different materials and the inapplicability of the PSF fitted to one material to return good deblurring results on another material.

3.6.3 New Data Acquisitions

New data were recently acquired at the Nevada National Security Site device assembly facility. Three realistic objects were interrogated with both neutron API and high-energy x-ray radiography. Once access to these data is available, the material estimation algorithm will be tested with the new data. A considerable complication with these data is that the x-ray source and detector are different than what has been used in previous measurement campaigns. This difference makes quantitative material measurements difficult, but preliminary results are likely to indicate the feasibility of using such algorithms for analyzing data of large and dense objects.

4. PROGRESS ON MATERIAL IDENTIFICATION USING COMBINED ENERGY/FLIGHT-TIME ANALYSIS

The present effort addresses identifying material compositions of a known geometry inferred from analysis of an image. Most approaches to analyzing API neutron data isolate single observables such as neutron transmission, elastic scattering, inelastic collisions and emitted neutrons or gamma rays, (*n*, *xn*) reaction neutrons, or induced-fission neutrons or gamma rays. Individual observables like these are insufficient to the task of identifying materials, but more complicated observables, such as the energy- and time-dependent neutron current may provide sufficient information.

When attempting to identify materials in an inspected object, simultaneously fitting signatures and evaluating all combinations of materials and geometries of the inspected object is desirable. Evaluation of many combinations of materials will require approximate forward transport that is fast enough to perform the ensemble of calculations in minutes.

The initial thrust of this effort was to identify means of implementing this fast forward model, and in FY 2020, North Carolina State University (NCSU) began developing a method for accelerating transport calculations using precomputed voxel *transfer functions* (also known as an impulse response or Green's functions). Initial development concentrated on predicting the emergent energy distribution. Subsequent efforts concentrated on predicting the emergent energy and time-dependent neutron current and evaluating whether this combined information was sufficient to identify the order of 1D material slabs of a known material list.

4.1 CALCULATING ENERGY- AND TIME-DEPENDENT NEUTRON CURRENT

During FY 2022, NCSU reformulated the way they calculate neutron current emerging from a voxel vs. time and energy to use an *inner product* operation over energy and a *convolution* operation over time-delay:

$$J_{\mathrm{out}}(E_{\mathrm{out}}, t_{\mathrm{out}}) = \int dE_{\mathrm{in}} \int d\tau \; H(E_{\mathrm{out}}, \tau \,; E_{\mathrm{in}})\, J_{\mathrm{in}}(E_{\mathrm{in}}, t_{\mathrm{in}} = t_{\mathrm{out}} - \tau).$$

Here, J_{out} denotes the emergent current as a function of energy E_{out} and time t_{out}; J_{in} is the incident current as a function of energy E_{in} and time $t_{\mathrm{in}} = t_{\mathrm{out}} - \tau$; and H denotes the transfer function that accounts for the change in neutron energy $E_{\mathrm{in}} \rightarrow E_{\mathrm{out}}$ within the voxel and the time-delay $\tau = t_{\mathrm{out}} - t_{\mathrm{in}}$ for neutrons traveling through the voxel. The previous formulation, which used an inner product over both energy and time, could not correctly calculate transit time for neutrons traversing multiple, coupled voxels. The new formulation correctly calculates transit time.

The transfer function for a given voxel composition is accumulated by histogramming particle tracks incident on and emergent from the voxel vs. incident and emergent energy and time using the MCNP6.2 `ptrac` particle tracking output:

$$H(E_{\mathrm{out}}, \tau; E_{\mathrm{in}}) = \frac{J_{\mathrm{out}}(E_{\mathrm{out}}, \tau = t_{\mathrm{out}} - t_{\mathrm{in}}; E_{\mathrm{in}})}{J_{\mathrm{in}}(E_{\mathrm{in}})},$$

where $J_{\mathrm{in}}(E_{\mathrm{in}}) = \int dt_{\mathrm{in}} \; J_{\mathrm{in}}(E_{\mathrm{in}}, t_{\mathrm{in}})$ is the incident current versus energy; the transit time-delay τ depends only on the incident energy, not on the absolute incident time. The normalization divides the elements of the tensor $J_{\mathrm{out}}(E_{\mathrm{out}}, \tau; E_{\mathrm{in}})$ row-wise over incident energy.

The transfer function for a given 1D voxel is further partitioned according to (a) neutrons that traveled through the voxel *uncollided*; (b) *transmitted* neutrons that collided in the voxel and emerged from the side opposite the side through which they entered; (c) *reflected* neutrons that collided in the voxel and emerged from the same side through which they entered; and (d) *absorbed* neutrons that entered the voxel but did not emerge from it.

Voxel transfer functions were calculated for three different 1D slabs of material: highly enriched uranium (HEU) metal, polyethylene (poly), and iron; each slab was 1 cm thick. The transfer functions were accumulated using a pseudo-uniform neutron source term (first described in FY 2021), which is sampled from a logarithmically uniform distribution over energies between 10^{-11} and 1 MeV, and then it is sampled from a linearly uniform distribution over energies between 1 and 20 MeV. This source term was selected to sample both low- and high-energy neutrons with similar frequency in the accumulation of the voxel transfer functions; it is illustrated in Figure 28. Figure 29–Figure 31 show the voxel transfer functions vs. incident energy, emergent energy, and time delay for HEU metal, polyethylene, and iron, respectively.

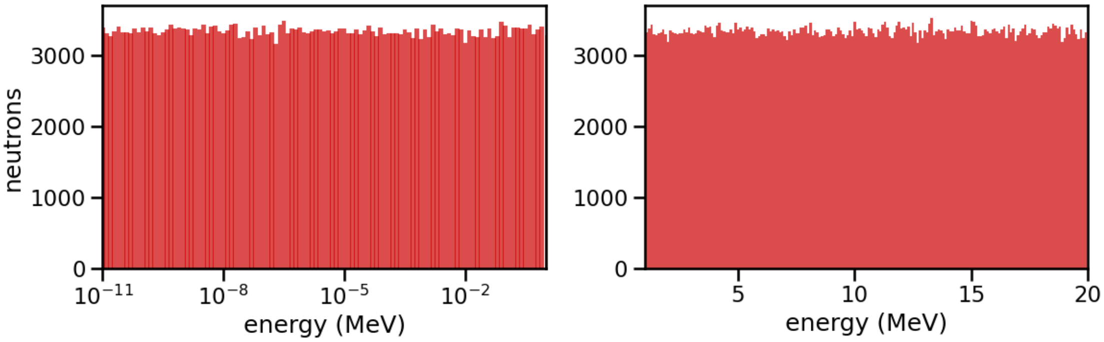

Figure 28. Pseudo-uniform neutron source term used to accumulate voxel transfer functions. (*left*) The source term is logarithmically uniform over 10^{-11} to 1 MeV, (*right*) and then it is linearly uniform over 1 to 20 MeV.

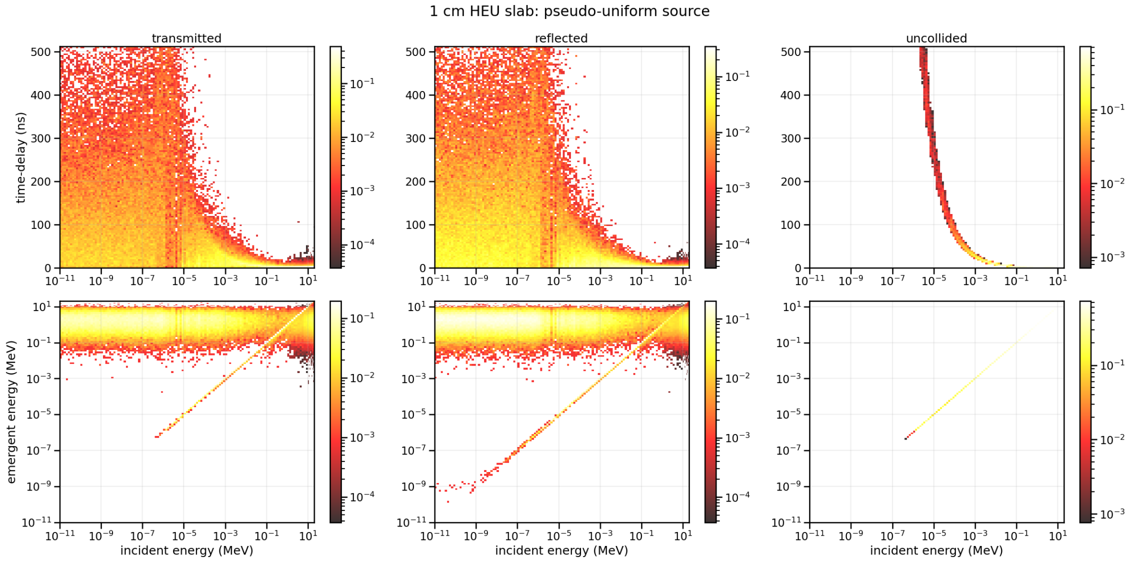

Figure 29. Voxel transfer function for HEU metal.

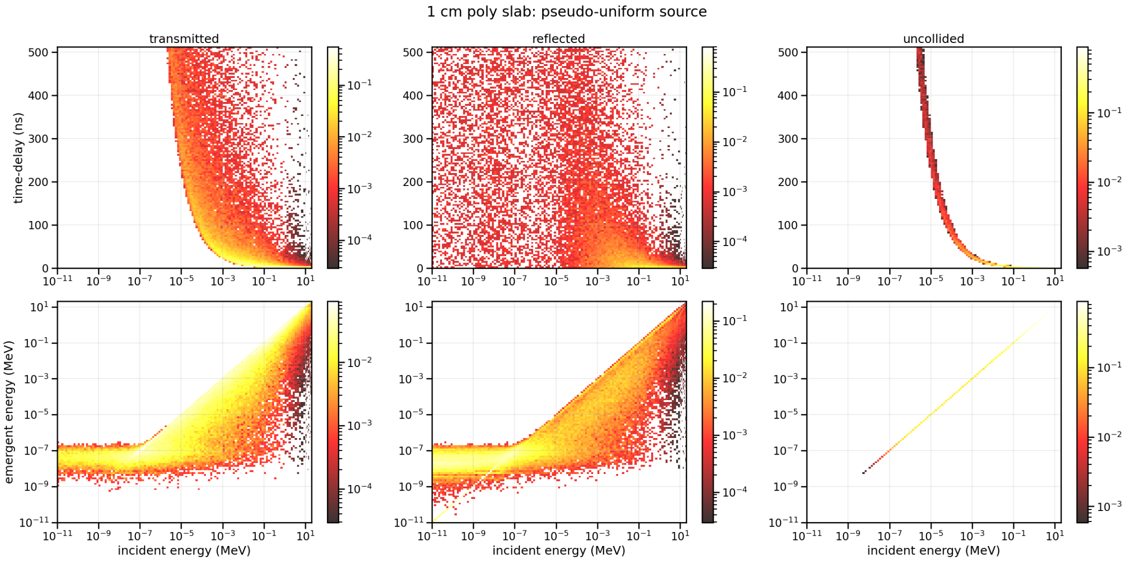

Figure 30. Voxel transfer function for polyethylene.

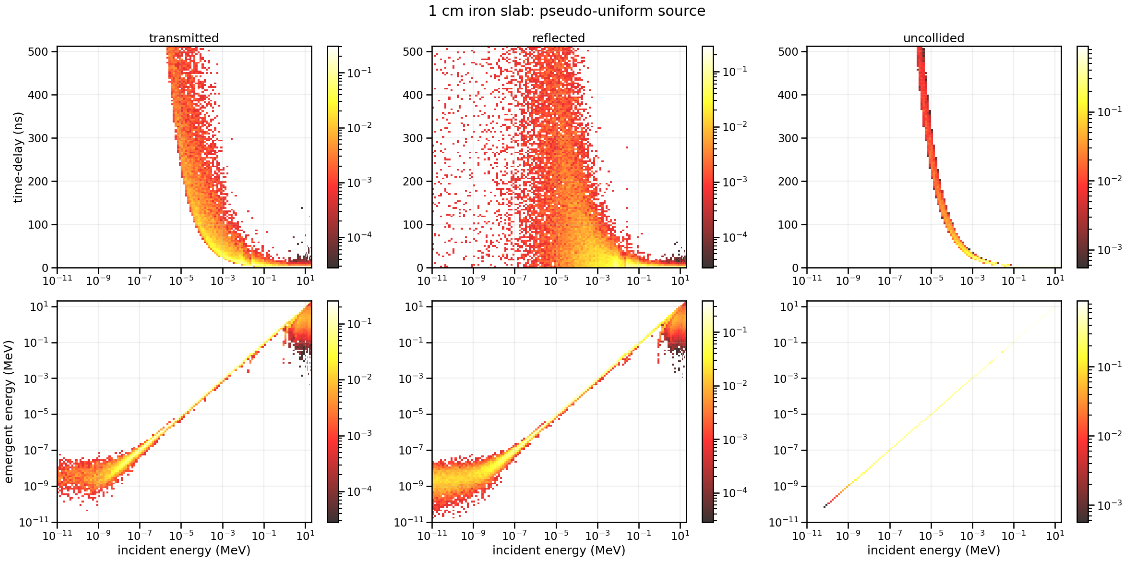

Figure 31. Voxel transfer function for iron.

Energy-dependent TOF calculations of the emergent neutron current for each material were tested using three different source terms: (1) the pseudo-uniform neutron spectrum, (2) a fission neutron spectrum, and (3) a 14 MeV D-T neutron spectrum. Figure 32–Figure 40 show the emergent current vs. energy and TOF for HEU metal, polyethylene, and iron, respectively, for each incident neutron spectrum. Each calculation reproduces the emergent current reasonably well, although not perfectly for the fission neutron and 14 MeV D-T neutron incident spectra.

The calculation of emergent current using the pseudo-uniform incident spectrum demonstrated that the calculations are numerically accurate when the incident spectrum is identical to the source term used to accumulate the transfer function. For the fission neutron and 14 MeV D-T neutron incident spectra, the calculations illustrated the magnitude of the error in estimated emergent current when the incident spectrum differs from the source term used to accumulate the voxel transfer function. These errors are most likely principally caused by the difference in the neutron histories used to accumulate the transfer function vs. those used to calculate the emergent current.

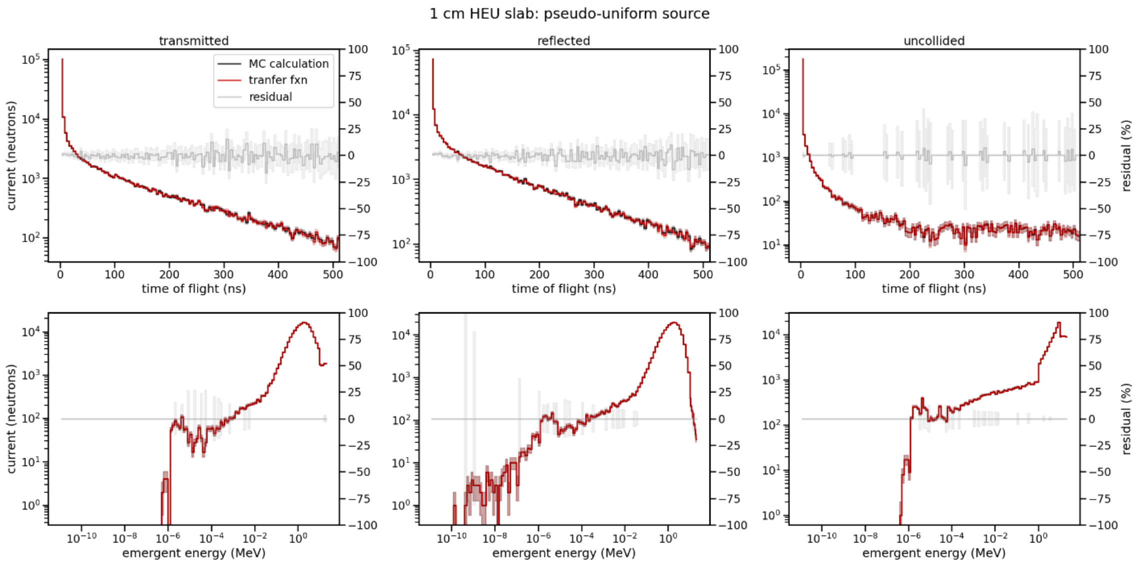

Figure 32. Calculation of emergent current for HEU metal using the pseudo-uniform source term to accumulate the voxel transfer function and the same incident spectrum, compared with the MCNP simulation of emergent current.

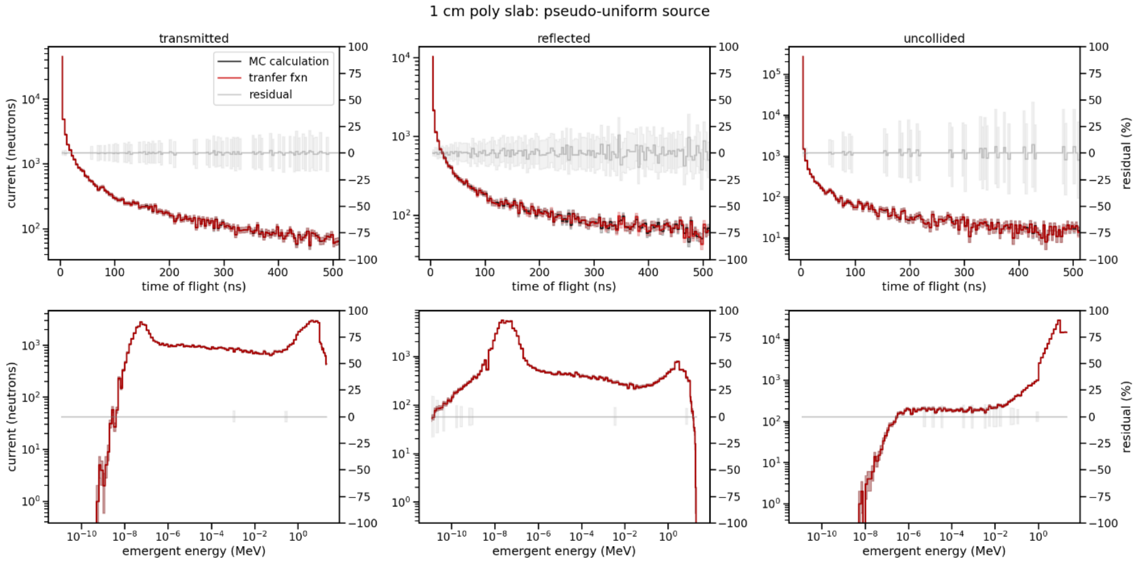

Figure 33. Calculation of emergent current for polyethylene using the pseudo-uniform source term to accumulate the voxel transfer function and the same incident spectrum, compared with the MCNP simulation of emergent current.

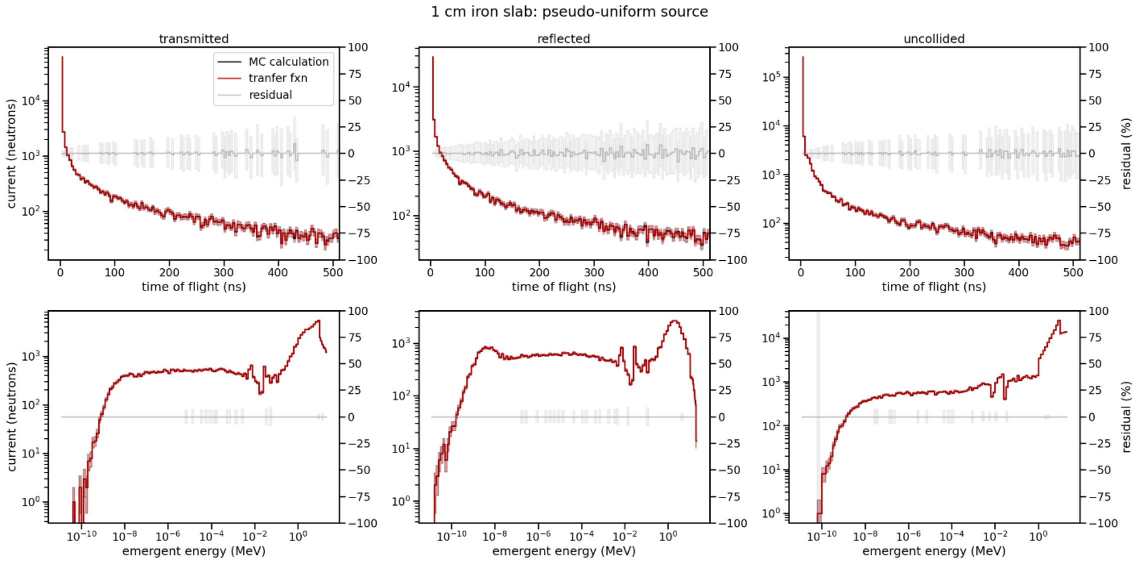

Figure 34. Calculation of emergent current for iron using the pseudo-uniform source term to accumulate the voxel transfer function and the same incident spectrum, compared with the MCNP simulation of emergent current.

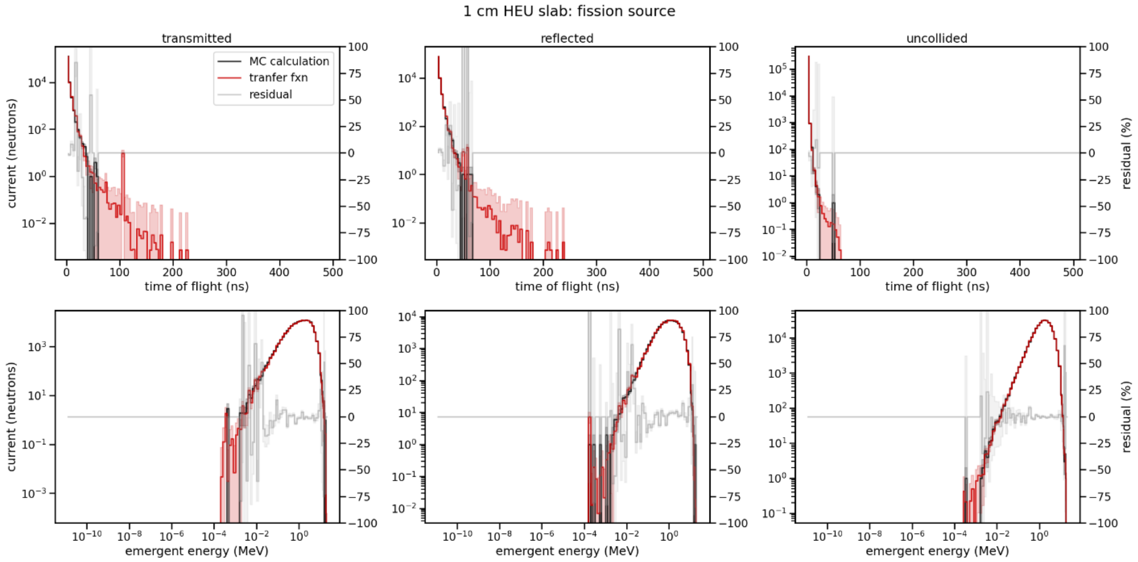

Figure 35. Calculation of emergent current for HEU metal using the pseudo-uniform source term to accumulate the voxel transfer function and a fission neutron incident spectrum, compared with the MCNP simulation of emergent current.

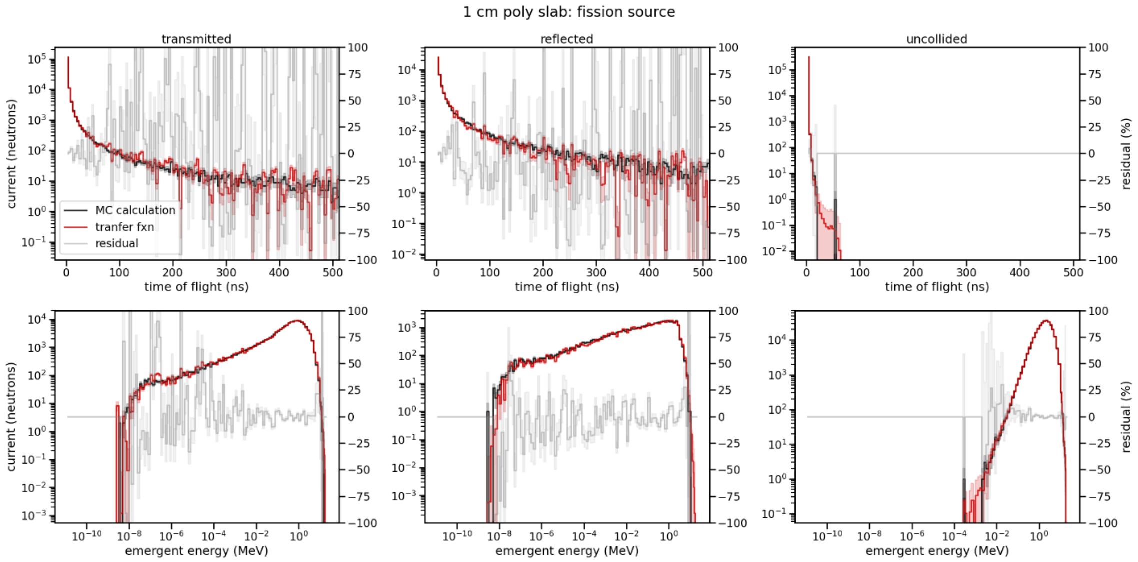

Figure 36. Calculation of emergent current for polyethylene using the pseudo-uniform source term to accumulate the voxel transfer function and a fission neutron incident spectrum, compared with the MCNP simulation of emergent current.

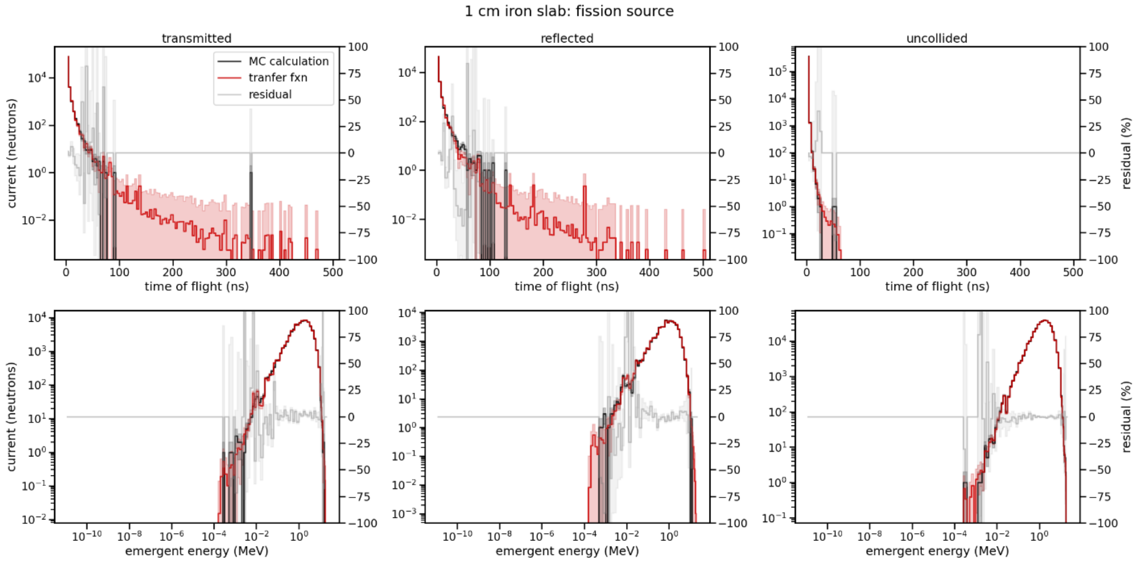

Figure 37. Calculation of emergent current for iron using the pseudo-uniform source term to accumulate the voxel transfer function and a fission neutron incident spectrum, compared with the MCNP simulation of emergent current.

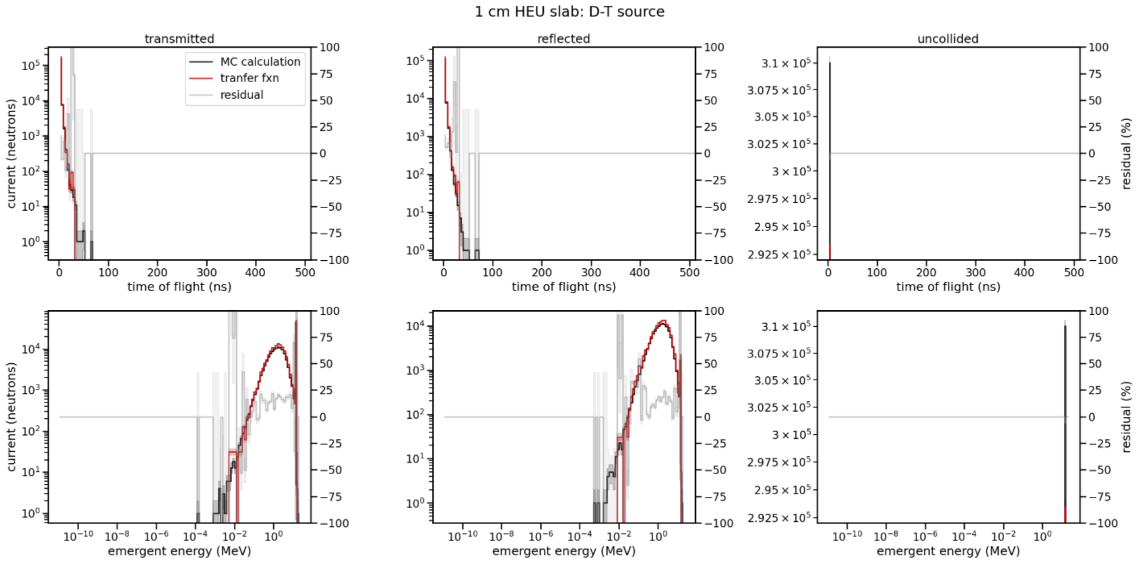

Figure 38. Calculation of emergent current for HEU metal using the pseudo-uniform source term to accumulate the voxel transfer function and a 14 MeV D-T neutron incident spectrum, compared with the MCNP simulation of emergent current.

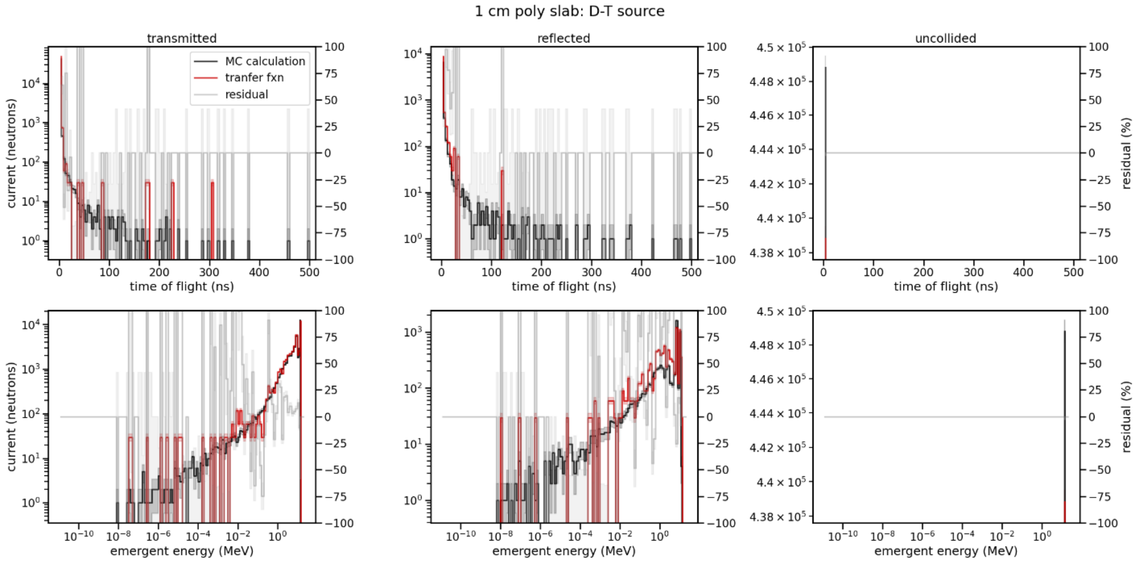

Figure 39. Calculation of emergent current for polyethylene using the pseudo-uniform source term to accumulate the voxel transfer function and a 14 MeV D-T neutron incident spectrum, compared with the MCNP simulation of emergent current.

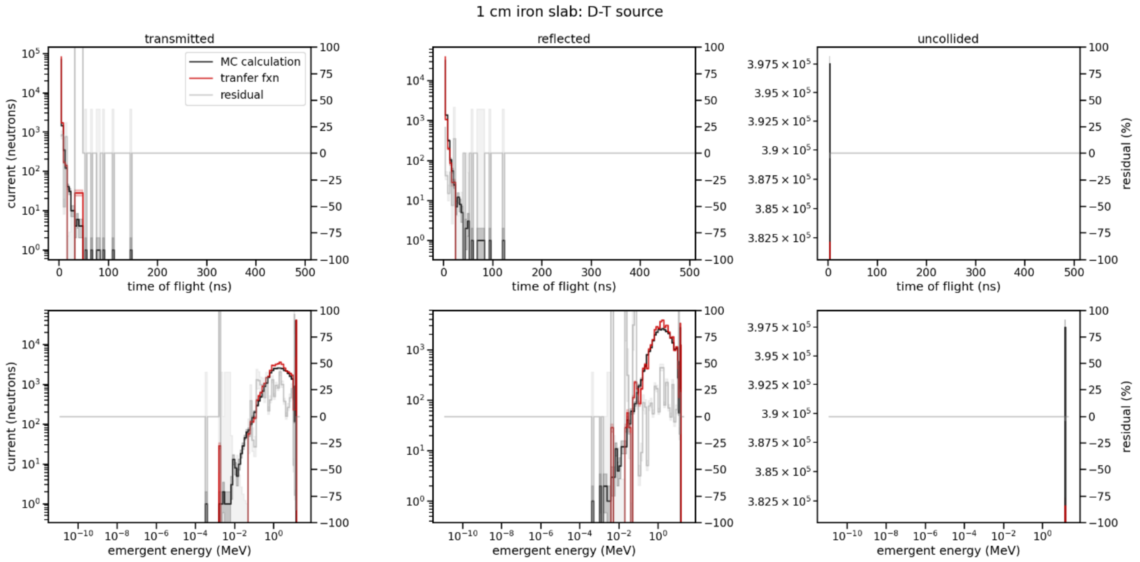

Figure 40. Calculation of emergent current for iron using the pseudo-uniform source term to accumulate the voxel transfer function and a 14 MeV D-T neutron incident spectrum, compared with the MCNP simulation of emergent current.

4.2 COUPLING MULTIPLE VOXELS

During FY 2022, NCSU also implemented transfer function calculations of energy- and time-dependent neutron current for multiple, coupled voxels. The initial approach is illustrated in Figure 41. The current emergent from a series of coupled voxels is estimated by sequentially applying the transfer function of each successive voxel to the current emergent from the previous voxel.

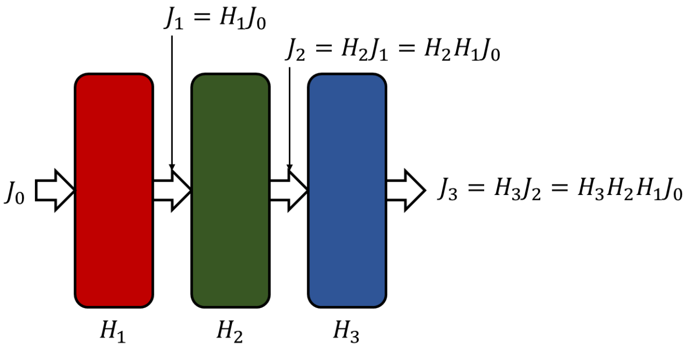

Figure 41. Coupling multiple voxel transfer functions.

The calculation illustrated in Figure 41 only accounts for uncollided and transmitted neutrons (and, implicitly, neutrons absorbed in each voxel). It neglects the contribution of neutrons that are reflected from a voxel back into the previous voxel and then reflected back again from that previous voxel. This approximation introduces systematic errors into the voxel transfer function calculations, which can negatively affect the identification of voxel composition. The next section of this report describes the method NCSU developed to approximately account for reflection.

Figure 42 and Figure 43 show the energy- and time-dependent emergent neutron current estimated for three coupled, 1D voxels composed of HEU metal, polyethylene, and iron (in that order left-to-right). Each voxel was 1 cm thick, and the neutron source-term was pseudo-uniformly distributed over 10^{-11} to

20 MeV, as illustrated in Figure 28. Figure 42 and Figure 43 compare the current estimated using voxel transfer functions with the MCNP simulation of emergent current. The voxel transfer function calculations generally preserve the distribution of emergent neutrons over energy and TOF, but they exhibit significant systematic errors, particularly for low energy and long flight time.

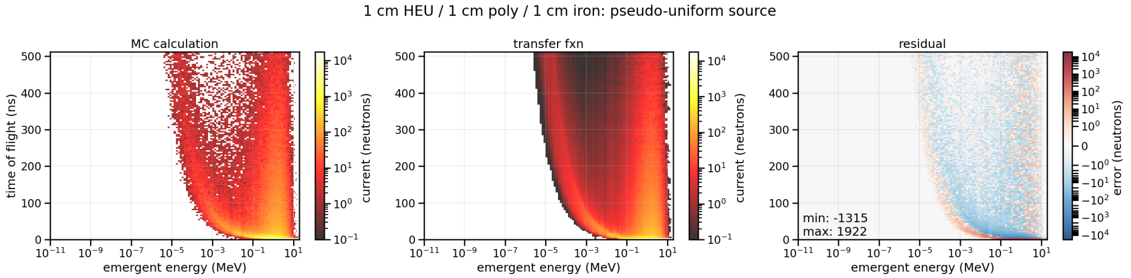

Figure 42. Emergent neutron current estimated using voxel transfer functions vs. the original MCNP simulation; the source term was pseudo-uniformly distributed over 10^{-11} to 20 MeV. The left histogram shows the original MCNP simulation, the middle histogram shows the voxel transfer function estimate, and the right histogram shows the error in the voxel transfer function estimate

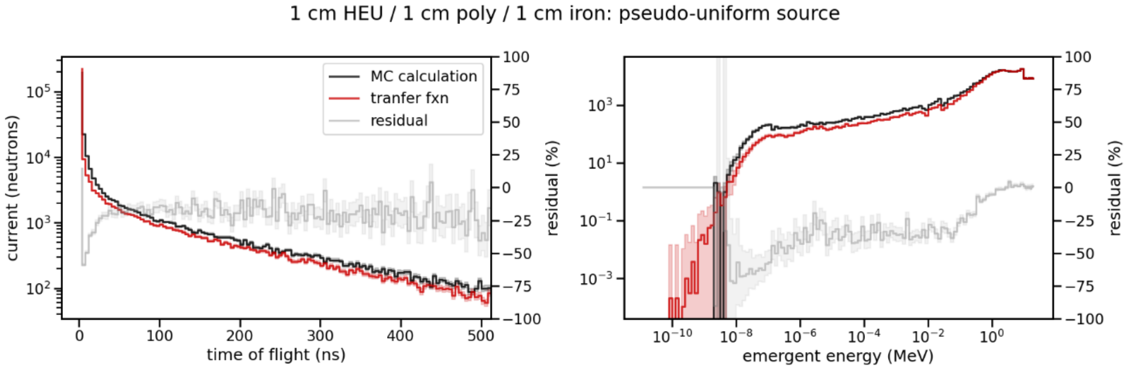

Figure 43. Emergent neutron current vs. (*left*) time of flight and (*right*) energy for calculation shown in Figure 42. The black histograms show the original MCNP simulation, the red histograms show the voxel transfer function estimate, and the gray histograms show the relative error in the transfer function estimate

The discrepancy between the voxel transfer function and MCNP simulations becomes more substantial when the neutron source term is sampled from a fission spectrum, as Figure 44 and Figure 45 demonstrate. In this case, the transfer function calculation did not reproduce the ridge centered at about 1 MeV that is evident in the energy vs. flight-time histogram of the emergent current. This feature is caused by fission induced in the HEU voxel, and its absence in the voxel transfer function calculation indicates that, because the voxel transfer function calculation neglected neutron reflection, it could not account for neutrons that are reflected by the polyethylene voxel back into the HEU voxel, where they subsequently induce fission. The absence of this feature was most likely not evident in the calculation shown in Figure 42 because, in that case, fission was principally induced by low-energy neutrons in the pseudo-uniform source incident on the HEU voxel.

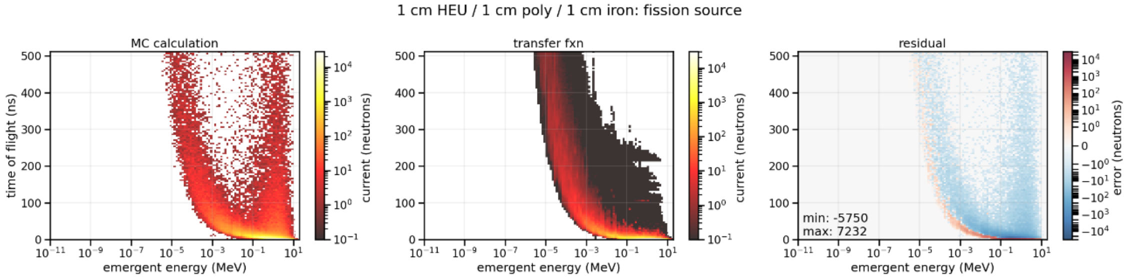

Figure 44 Emergent neutron current estimated using voxel transfer functions vs. the original MCNP simulation; the source term was a fission spectrum. (*left*) The original MCNP simulation, (*center*) the voxel transfer function estimate, and (*right*) the error in the voxel transfer function estimate

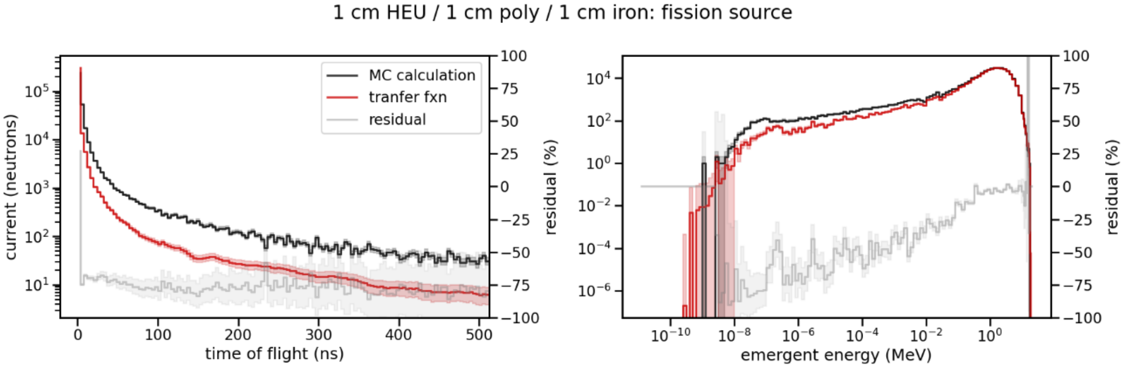

Figure 45. Emergent neutron current vs. (*left*) TOF and (*right*) energy for calculation shown in Figure 44 and Figure 42. The black histograms show the original MCNP simulation, the red histograms show the voxel transfer function estimate, and the gray histograms show the relative error in the transfer function estimate

4.3 ACCOUNTING FOR NEUTRON REFLECTION

NCSU evaluated two alternative iterative methods to account for the effect of neutron reflection on the emergent current. Ultimately, the iterative scheme illustrated in Figure 46 was chosen as the better approximation. In the figure, T_n denotes the transfer function for transmitted (and uncollided) neutrons for voxel n, and R_n denotes the transfer function for reflected neutrons. For each current J_n^q shown, n denotes the voxel to the left, and q denotes the pass through the iterative scheme. As the figure illustrates, this scheme computes the reflection of neutrons back and forth between adjacent voxels, instead of computing the transmission of neutrons through all the voxels and then computing their reflection back to the first voxel. NCSU found that this latter scheme was not as accurate an approximation as the one shown in Figure 46, which was ultimately implemented. NCSU found that the iterative scheme illustrated in Figure 46 converges to a stable solution for the emergent current in a few iterations.

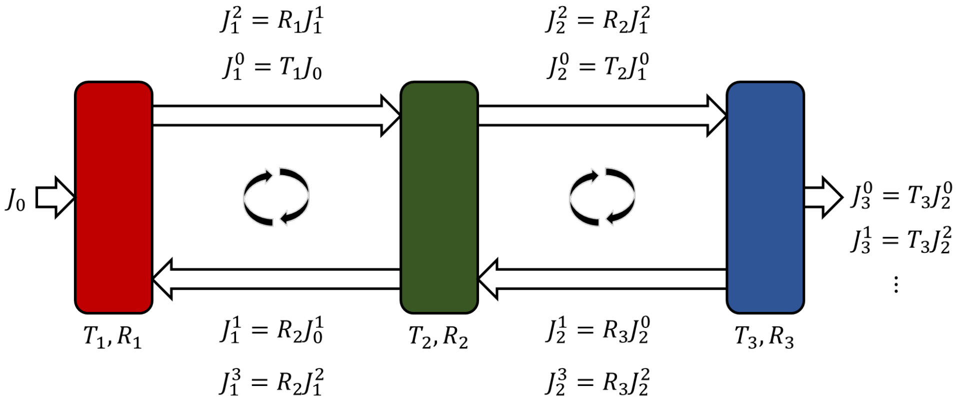

Figure 46. Iterative scheme to account for neutron reflection.

Initially, this approximation was implemented and tested to evaluate its accuracy for predicting the energy-dependent emergent neutron current. NCSU constructed test cases for all six possible orderings of three voxels in which one voxel was composed of HEU metal, another was composed of polyethylene, and the remaining voxel was composed of iron. Figure 47 compares the emergent neutron current computed using voxel transfer functions with that computed directly by MCNP; the title above each subplot notes the voxel ordering and the root mean square error (RMSE) between the voxel transfer function calculation and the corresponding MCNP simulation. In these tests, the voxel transfer function calculations accounted for reflected neutrons using the iterative scheme illustrated in Figure 46. For the six test cases shown in Figure 47, the iterative scheme to account for neutron reflection reproduces the MCNP simulation with moderate accuracy, although some systematic error remains. However, the voxel transfer function calculations are orders of magnitude faster than the MCNP simulations.

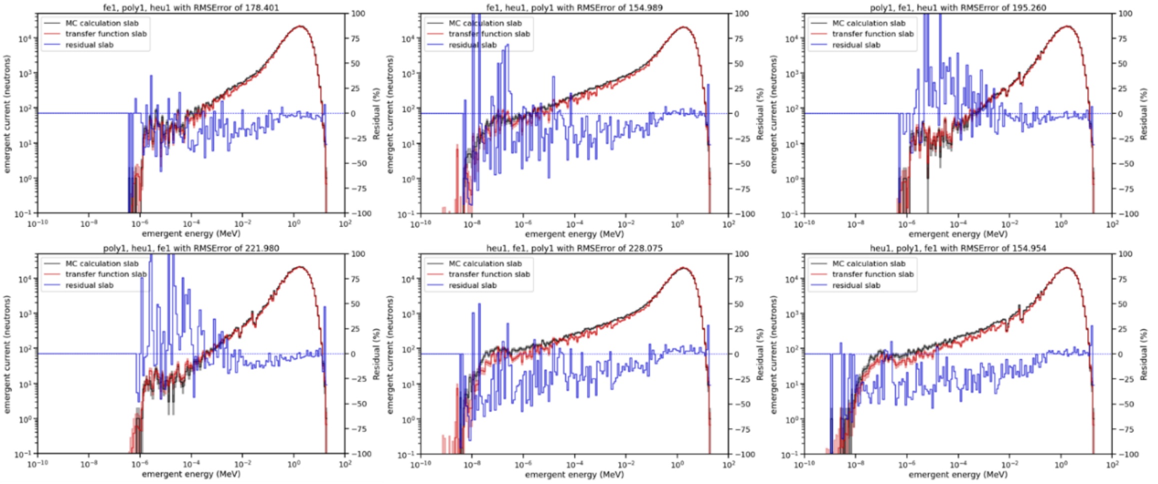

Figure 47. Comparison of MCNP simulations and voxel transfer function calculations of neutron current emergent from the right face of three coupled voxels composed of HEU metal, polyethylene, and iron. Fission spectrum neutrons were incident on the left face.

NCSU subsequently implemented an augmented version of the scheme to account for reflection in the energy- and time-dependent neutron current. Figure 48 shows the energy- and time-dependent emergent current computed for a fission spectrum source term using voxel transfer function calculations corrected to account for neutron reflection. It reproduces the MCNP simulation more accurately, including the ridge centered at about 1 MeV resulting from fission induced in the HEU voxel by neutrons reflected from the polyethylene voxel.

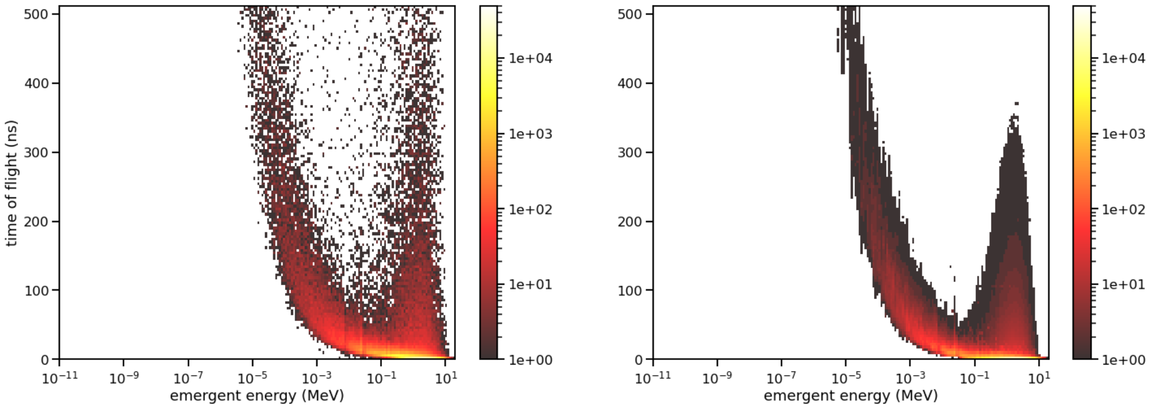

Figure 48. Emergent neutron current estimated using voxel transfer functions vs. the original MCNP simulation. (*left*) The original MCNP simulation and (*right*) the voxel transfer function estimate, including correction for neutron reflection.

4.4 VOXEL COMPOSITION IDENTIFICATION

In FY 2022, NCSU also compared voxel transfer function calculations (including corrections for reflected neutrons) of the energy- and time-dependent neutron current emergent from three coupled 1D 1 cm thick voxels composed of HEU metal, polyethylene, and iron. The emergent neutron current was calculated for all six possible orderings of the coupled voxels, and the transfer function calculations were compared with an MCNP simulation for the case in which the voxels are HEU metal, polyethylene, and iron, in that order left-to-right. Those comparisons are shown in Figure 49. The voxel ordering is shown in the title of each subplot, and the histogram color scale shows the residual between the MCNP simulation and the transfer function calculation. Positive residuals (red on the color scale) occur when the transfer function calculation overpredicts the MCNP simulation; conversely, negative residuals (blue on the color scale) occur where the transfer function calculation underpredicts the MCNP simulation. The closest match, in terms of the RMSE, occurs for the correct ordering: HEU-polyethylene-iron.

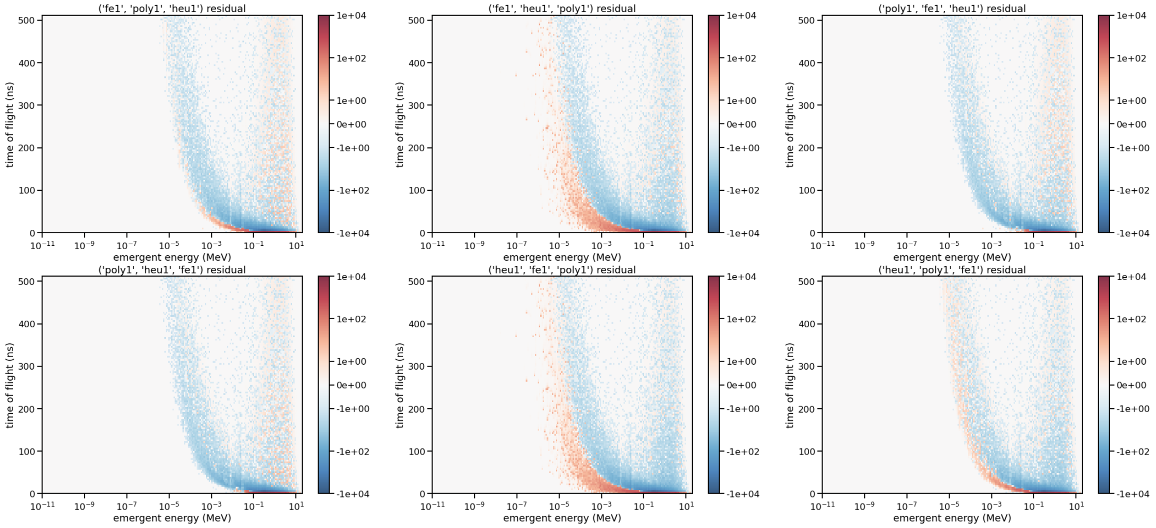

Figure 49. Comparison of MCNP simulations of current emergent from the right face of three coupled voxels composed of HEU metal, polyethylene, and iron (in that order, left-to-right) with transfer function calculations for all six possible orderings of the voxels. The histogram color scale shows the residual between the MCNP simulation and the transfer function calculation.

However, one alternative ordering (HEU-iron-polyethylene) results in a comparably low RMSE, as Figure 50 illustrates. To the eye, the residuals for the incorrect ordering (on the left) appear to be consistently smaller than the residuals for the correct ordering (on the right), except for the two narrow valleys near 100 keV neutron energy. These features are likely caused by resonances in the absorption cross section of one or more of the iron isotopes. The residual for the correct ordering is small in the vicinity of these features (which is expected), and it is substantially larger for the incorrect ordering. The larger residuals near these two features may be primarily responsible for the larger RMSE. NCSU is currently investigating several error metrics alternatives to the RMSE, including the mean absolute percentage error, the RMS relative error, and the RMS error in the log of the neutron current, to determine which metric best reflects the behavior of the energy- and time-dependent residuals.

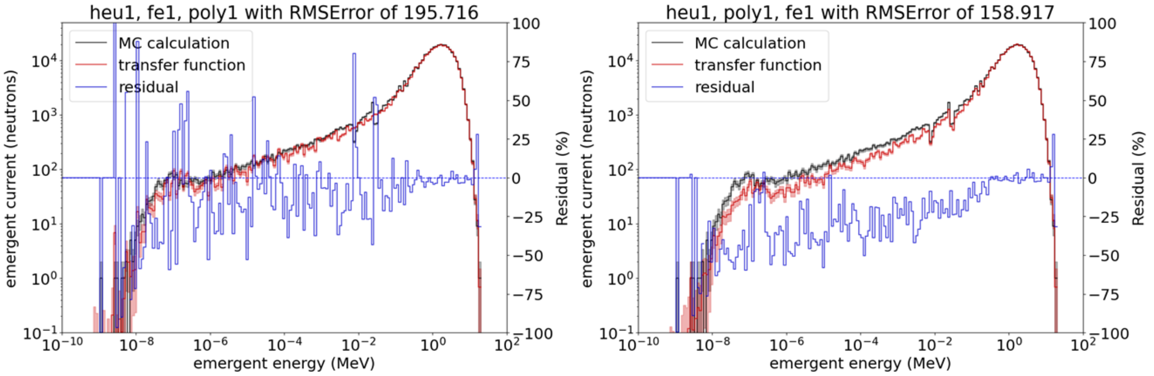

Figure 50. Comparison of the energy-dependent neutron current emergent from three voxels composed of HEU metal, iron, and polyethylene (in that order) to the correct ordering, HEU metal, polyethylene, and iron. The MCNP simulation is for the correct ordering in both cases.

4.5 PLANS FOR FY2023 Q1

In FY 2023 Q1, NCSU will continue to evaluate alternative metrics and methods for voxel composition identification. They will also include additional candidate materials (e.g., DU and void) to test voxel identification methods for a broader set of materials.

5. REFERENCES

[1] P. A. Hausladen, M. A. Blackston, A. J. Gilbert, J. Gregor, and J. K. Mattingly. 2020. *Progress on Associated-Particle Imaging Algorithms, 2020*, ORNL/SPR-2020/1766. Oak Ridge, Tennessee: Oak Ridge National Laboratory.

[2] P. A. Hausladen, M. R. Heath, R. J. Newby, P. B. Rose, J. Gregor, A. J. Gilbert, L. A. Campbell, N. Deshmukh, R. S. Wittman, J. K. Mattingly, and M. Lockhart. 2021. *Progress on Associated-Particle Imaging Algorithms, 2021*, ORNL/SPR-2021/2253. Oak Ridge, Tennessee: Oak Ridge National Laboratory.

[3] B. Perot et al., 2007. “Development of the EURITRACK Tagged Neutron Inspection System.” *Nuclear Instruments and Methods in Physics Research Section B* 261: 295–298.

[4] L. Nakae et al. 2018. *Fast Time-of-Flight Correlation System—End-of-Year Report FY 2018*. LLNL-AR-763682. Livermore, California: Lawrence Livermore National Laboratory.

[5] P. Hausladen, M. Blackston, and J. Gregor. 2019. *Progress Update on Iterative Reconstruction of Neutron Tomographic Images*. ORNL/SPR-2019/1353. Oak Ridge, Tennessee: Oak Ridge National Laboratory.

[6] S. Rose, M. Andersen, E. Sidky, and X. Pan. 2015. “Noise Properties of CT Images Reconstructed by Use of Constrained Total-Variation Data-Discrepancy Minimization.” *Medical Physics* 42: 2690–2698.

[7] J. Gregor, P. Bingham, and L. F. Arrowood. 2016. “Total Variation Constrained Weighted Least Squares Using SIRT and Proximal Mappings.” 4th International Conference on Image Formation in X-ray Computed Tomography, Bamberg, Germany, July 2016.

[8] A. Chambolle and T. Pock. 2011. “A First-Order Primal-Dual Algorithm for Convex Problems with Applications to Imaging.” *Journal of Mathematical Imaging and Vision* 41 (1): 120–145.

[9] J. Gregor and J. A. Fessler. 2015. “Comparison of SIRT and SQS for Regularized Weighted Least Squares Image Reconstruction.” *IEEE Transactions on Computational Imaging* 1 (1): 44–55.

[10] Y. Nesterov. 1983. “A method for unconstrained convex minimization problem with the rate of convergence $O(1/k^2)$.” *Dokl. Akad. Nauk. USSR* 269: 543–547.

[11] D. Kim, S. Ramani, and J. A. Fessler. 2013. “Accelerating X-ray CT ordered subsets image reconstruction with Nesterov’s first-order methods.” Intl. Meeting on Fully 3D Image Reconstruction in Radiology and Nuclear Medicine, Lake Tahoe, California. June 16–21, 2013.

[12] D. Kim and J. A. Fessler. 2016. “Optimized first-order methods for smooth convex minimization.” *Math. Programming* 159: 81–107.

[13] D. Kim and J. A. Fessler. 2017. “On the convergence analysis of the optimized gradient methods.” *J. Optim. Theory Appl.* 172: 187–205.

[14] D. Kim and J. A. Fessler. 2018. “Adaptive restart of the optimized gradient method for convex optimization.” *J. Optim. Theory Appl.* 178: 240–263.

[15] M. R. Heath et al. 2022. “Development of a Portable Pixelated Fast-Neutron Imaging Panel.” *IEEE Transactions on Nuclear Science* 69 (6): 1352–1356. https://doi.org/10.1109/TNS.2021.3136344.

[16] A. J. Gilbert, B. S. McDonald, S. M. Robinson, K. D. Jarman, T. A. White, and M. R. Deinert. 2014. “Non-Invasive Material Discrimination Using Spectral X-Ray Radiography.” *Journal of Applied Physics* 115 (15): 154901..

[17] A. J. Gilbert, B. S. McDonald, and M. R. Deinert. 2016. “Advanced Algorithms for Radiographic Material Discrimination and Inspection System Design.” *Nuclear Instruments and Methods in Physics Research Section B* 385: 51–58.

[18] M. A. Blackston and P. A. Hausladen. 2015. “Fast-Neutron Elastic-Scatter Imaging for Material Characterization.” 2015 IEEE Nuclear Science Symposium and Medical Imaging Conference (NSS/MIC), San Diego, California. October 31–November 7, 2015.

[19] B. Canion, S. McConchie, and S. Landsberger. 2017. “Source Correlated Prompt Neutron Activation Analysis for Material Identification and Localization.” *IEEE Transactions on Nuclear Science* 64 (7): 1725–1732.

[20] P. A. Hausladen et al. 2010. “Induced-Fission Imaging of Nuclear Material.” *INMM 51st Annual Meeting*, pp. 1–10, Baltimore, Maryland, July 11–15, 2010.

[21] A. J. Gilbert, L. W. Campbell, N. Deshmukh, and R. S. Wittman. 2021. “Radiography scatter estimation for accurate material quantification.” In *IEEE Nuclear Science Symposium and Medical Imaging Conference*, 2021.

[22] B. Ohnesorge, T. Flohr, and K. Klingenbeck-Regn. 1999. ”Efficient object scatter correction algorithm for third and fourth generation CT scanners.” *European Radiology* 9 (3): 563–569.

[23] J. T. Goorley, M. R. James, T. E. Booth, F. B. Brown, J. S. Bull, L. J. Cox, J. W. Durkee, Jr., J. S. Elson, M. L. Fensin, R. A. Forster, III, J. S. Hendricks, H. G. Hughes, III, R. C. Johns, B. C. Kiedrowski, R. L. Martz, S. G. Mashnik, G. W. McKinney, D. B. Pelowitz, R. E. Prael, J. E. Sweezy, L. S. Waters, T. Wilcox, and A. J. Zukaitis (2012). "Initial MCNP6 Release Overview - MCNP6 version 1.0." Nuclear Technology, 180:3, 298-315, DOI: 10.13182/NT11-135.

[24] E. Roessl and C. Herrmann. 2009. "Cramer-Rao lower bound of basis image noise in multiple-energy x-ray imaging." *Physics in Medicine and Biology* 54 (5): 1307.

[25] Kyle Schmitt, personal communication, September 2022.